Title

Analysis of fluorescent calcium signals in the detection of neural circuitry abnormalities in a mouse model of autism

Author

Cantu, Daniel Alejandro

Publication Date

2019

Peer reviewed|Thesis/dissertation

UNIVERSITY OF CALIFORNIA

Los Angeles

Analysis of fluorescent calcium signals in the detection of neural circuitry abnormalities in a mouse model of autism

A dissertation submitted in partial satisfaction of the

requirements for the degree Doctor of Philosophy

in Neuroscience

by

Daniel Alejandro Cantú

2019

ABSTRACT OF THE DISSERTATION

Analysis of fluorescent calcium signals in the detection of neural circuitry abnormalities in a mouse model of autism

by

Daniel Alejandro Cantú

Doctor of Philosophy in Neuroscience

University of California, Los Angeles, 2019

Professor Carlos Portera-Cailliau, Chair

The formation, refinement and plasticity of circuits are defining features of the central nervous system, giving rise to many of the unique and complex functionalities of the brain. Advances in dynamic fluorescence imaging technology are allowing an increasing number of researchers to investigate the activity of neural circuits *in vivo* in animal models. Unfortunately, deciphering the data obtained through these methods is time consuming and has largely been delegated to a few investigators who have the expertise to do so. We present an open-source, modular, and adaptable software suite designed for motion correction, segmentation, signal extraction, and deconvolution of fluorescent calcium imaging data. We apply this *EZcalcium* toolbox to the analysis of calcium imaging data in a mouse model of autism in order to investigate the underlying neural circuit abnormalities in the primary somatosensory and visual cortices. These

contributions to the field of autism research demonstrate the utility of investigating neural circuits through optical methods.

The dissertation of Daniel Alejandro Cantú is approved.

Michele A. Basso

Dean Buonomano

Jack L. Feldman

Dario L. Ringach

Carlos Portera-Cailliau, Committee Chair

University of California, Los Angeles

2019

Table of Contents

List of Figures

Acknowledgements

I would like to thank my committee members Michele Basso, Dean Buonomano, Jack Feldman, Dario Ringach, and Carlos Portera-Cailliau for their knowledge, wisdom, patience, and support. You all pushed me to grow as a scientist and as a person and I will always be grateful for you contributions to my life.

The contents of Chapter 1 are derived from a manuscript in preparation titled "EZcalcium: A comprehensive and user-friendly toolbox for analysis of fluorescence calcium signals," of which I am the lead author. The complete author list is: Daniel Cantú, Cynthia He, Anubhuti Goel, Bo Wang, Anand Suresh, Nazim Kourdougli, William Zeiger, Erica D. Arroyo, and Carlos Portera-Cailliau. I led the writing of the MATLAB code for this project, with contributions and editing from Cynthia, Anubhuti, and Bo. Cynthia, Anubhuti, Anand, Nazim, Will, and Erica provided calcium imaging data, performed testing, and provided feedback. Carlos and I wrote the manuscript. I would also like to thank Eftychios Pnevmatikakis, Josh Vogelstein, Patrick Minault, Tsai-Wen Chen, and countless other programmers for making their own algorithms freely available so that they could be be incorporated in the EZcalcium toolbox.

The contents of Chapter 2 are adapted from two manuscripts in which I was the 2nd author. The first manuscript is "Tactile Defensiveness and Impaired Adaptation of Neuronal Activity in the Fmr1 Knock-Out Mouse Model of Autism" (He et al., 2017). The complete author list is: Cynthia He, Daniel Cantú, Shilpa Mantri, William Zeiger, Anubhuti Goel, Carlos Portera-Cailliau. With Cynthia, I wrote the MATLAB code for data analysis as the MATLAB code for generating a

whisker stimulus and synchronizing it with calcium imaging. I also helped Cynthia design and configure the novel surgical procedure to inject viral vectors at birth and to implant cranial windows in neonatal mice necessary for the experiments (He et al., 2018). Cynthia and Carlos designed the research and wrote the manuscript. Cynthia, Shilpa, Anubhuti, and Carlos performed the data analysis.

Additional material from Chapter 2 is adapted from the manuscript "Impaired perceptual learning in a mouse model of Fragile X syndrome is mediated by parvalbumin neuron dysfunction and is reversible" (Goel et al., 2018). The complete author list is: Anubhuti Goel, Daniel A. Cantú, Janna Guilfoyle, Gunvant R. Chaudhari, Aditi Newadkar, Barbara Todisco, Diego de Alba, Nazim Kourdougli, Lauren M. Schmitt, Ernest Pedapati, Craig A. Erickson, and Carlos Portera-Cailliau. With Anubhuti, I wrote the MATLAB code for all data analysis, as well as the MATLAB code for generating a visual stimulus and synchronization with calcium imaging. Anubhuti and Carlos designed experiments with help from Janna, Lauren, Ernest, and Craig for the human students. Anubhuti developed the experiments for mice and humans. Experiments and analysis were performed by Anubhuti, Gunvant, Aditi, Barbara, Diego, Nazim, and Janna. Anu, Lauren, Ernest, Craig, and Carlos interpreted the data and wrote the manuscript.

I would like to thank Lauren Wierenga for contributing to an early version of the sensory stimulus and data analysis codes used in these two manuscripts. I would also like to thank Nuo Li, Tsai-Wen Chen, Simon Peron, and Karel Svoboda for providing valuable education and feedback on writing data analysis code and performing behavioral experiments.

My thesis work was supported by the Eugene V. Cota-Robles Fellowship, UCLA; and the Neural Microcircuits Training Grant, NIH T32-NS058280.

Vita

EDUCATION-
University of California Irvine, Irvine, California
B.S. Biological Sciences – June 2009

RESEARCH EXPERIENCE-
Dr. Carlos Portera-Cailliau
Detection and analysis of neural circuitry abnormalities in a mouse model of autism
UCLA, Los Angeles, CA
March 2012-Present

Dr. Karel Svoboda
Analysis of Neural Circuits Underlying Decision Making
Janelia Farm, Ashburn, VA
September 2014-November 2014

Dr. Rhiju Das
Using Citizen Science to Probe Questions in RNA Biology
Stanford University, Stanford, CA
June 2010-June 2011

Dr. Aileen Anderson
Effects of the Microenvironment on Human Central Nervous System Neural Stem Cells Transplanted to Treat Spinal Cord Injury
UC Irvine, Irvine, CA
September 2007-June 2010

Dr. Teresa Morales
Neuroprotective Effects of Lactation Against Kainic Acid-Induced Damage in the Dorsal Hippocampus
Instituto de Neurobiología, Universidad Nacional Autónoma de México, Juriquilla, Querétaro
June 2007-September 2007

Dr. Francisco Ayala
Dr. Luis Mota-Bravo
Antibiotic Resistance in Environmental Bacterial Isolates
UC Irvine, Irvine, CA
June 2006-June 2007

FELLOWSHIPS, HONORS, AND GRANTS-
National Institutes of Health:
Neural Microcircuits Training Grant (February 2014-2016)
Neural Microcircuits Diversity Committee (March 2014-2016)

National Science Foundation:
Graduate Research Fellowship Program – Honorable Mention (April 2012, April 2013)

University of California, Los Angeles:
Eugene Cota-Robles Fellowship (September 2011)

University of California, Irvine:
Minority Biomedical Research Support Student (Summer 2006-Spring 2007)
Minorities Health and Health Disparities International Research Training Scholar (Summer 2007)
Maximizing Access to Research Careers Scholar (Fall 2007-Fall 2008)

PUBLICATIONS

Daniel Cantú, Cynthia He, Anubhuti Goel, Bo Wang, Anand Suresh, Nazim Kourdougli, William Zeiger, Erica D. Arroyo, Carlos Portera-Cailliau. **EZcalcium: A comprehensive and user-friendly toolbox for analysis of fluorescence calcium signals.** Manuscript in preparation, 2019.

Anubhuti Goel, Daniel A. Cantú, Janna Guilfoyle, Gunvant R. Chaudhari, Aditi Newadkar, Barbara Todisco, Diego de Alba, Nazim Kourdougli, Lauren M. Schmitt, Ernest Pedapati, Craig A. Erickson, and Carlos Portera-Cailliau. **Impaired perceptual learning in Fragile X syndrome is mediated by parvalbumin neuron dysfunction and is reversible.** Nature Neuroscience. 24 September, 2018.

Cynthia He, Erica Arroyo, Daniel Cantú, Anubhuti Goel, Carlos Portera-Cailliau. **A versatile method for viral transfection of calcium indicator in the neonatal mouse brain**. Frontiers in Neural Circuits. 23 July, 2018.

Cynthia He, Daniel Cantú, Shilpa Mantri, William Zeiger, Anubhuti Goel, Carlos Portera-Cailliau. **Tactile Defensiveness and Impaired Adaptation of Neuronal Activity in the Fmr1 Knock-Out Mouse Model of Autism.** J Neurosci. Volume 37, Issue 27, 5 July, 2017, Pages 6475-6487

Jeehyung Lee, Wipapat Kladwang, Minjae Lee, Daniel Cantú, Martin Azizyan, Hanjoo Kim, Alex Limpaecher, Sungroh Yoon, Adrien Treuille, Rhiju Das. **RNA Design Rules from a Massively Multiplayer Laboratory**. Proc. Natl. Acad. Sci. U.S.A. Volume 111, Issue 6, 11 February 2014, Pages 2122-2127.

Verónica Cabrera, Daniel Cantú, Eugenia Ramos, América Vanoye-Carlo, Marco Cerbón, and Teresa Morales. **Lactation is a natural model of hippocampus neuroprotection against excitotoxicity.** Neuroscience Letters. Volume 461, Issue 2, 11 September 2009, Pages 136-139.

Introduction

Studying neural circuits

Unraveling the mysteries of the human brain will require a detailed and comprehensive understanding of the structure and function of neurons and their connections. Only then, will we begin to fathom how the central nervous system gives rise to so many of its unique and complex abilities, such as learning, language, creativity, or decision making (Wei et al., 2014, Li et al., 2015, Tanaka et al., 2018). In the history of neuroscience, tools to investigate neural signals have lagged behind those for studying neuroanatomy by many decades (Ugolini, 1995, Livet et al., 2007, Chung et al., 2013). As a result, our knowledge of how ensembles of neurons interact functionally to encode memories or perceive sensory inputs remains rudimentary, in comparison to how well the anatomical connectome or even molecular and biochemical pathways have been characterized. Furthermore, developing better treatments for neuropsychiatric disorders, especially those caused primarily by abnormal circuit activity (e.g., autism spectrum disorders, epilepsy, depression, schizophrenia) (Gibson et al., 2008, Thompson et al., 2015, Foster and Conn, 2017, Wang et al., 2017), will require a more sophisticated understanding of network function.

For several decades, the only approach for recording from neurons in animal models was to use electrodes inserted into the brain (Piccolino, 1997, Jun et al., 2017). However, this was limited by the invasive nature of the experiment and the fact that only few neurons could be recorded from at a time. Additionally, the identity of different neuronal subtypes could not easily be recognized and chronic longitudinal recordings (over days or weeks) were not feasible. In the 21st century, with the advent of powerful fluorescence microscopy techniques (e.g., two-photon microscopy, microendoscopes, mesoscopes) (Denk et al., 1990, Mehta et al., 2004, Sofroniew et al., 2016) and

novel fluorescence sensors of neuronal activity (Chen et al., 2013, Walker et al., 2013), imaging has emerged as one of the preferred methods for recording network dynamics in awake, behaving animals. Through the use of synthetic or genetically encoded fluorescence indicators, it is now possible to probe the dynamic signals of both neurons and astrocytes with calcium and voltage sensors (Antic and Zecevic, 1995, Chen et al., 2013), and even track neurotransmitter release (Masharina et al., 2012, Marvin et al., 2013).

There are several unique advantages of recording neural activity with fluorescent indicators. First, the activity of dozens, hundreds or even thousands of neurons can be simultaneously imaged with sub-cellular resolution (e.g., dendritic spines, boutons). Second, imaging allows one to record network activity in head-fixed or freely moving animals, providing a key link between circuit activity and behavior. Third, fluorescence imaging is much less invasive than traditional methods for recording the activity of large numbers of neurons (e.g., tetrodes, silicon probes). Fourth, it can be more easily combined with cell-type specific genetic manipulations, which makes it possible to not only record from specific identified cell populations (e.g., brain region-, cortical layer-specific, or interneuron subtype-specific Cre lines), but also combine with other approaches to manipulate network activity, such as optogenetics (Ernst et al., 2008) and glutamate uncaging (Pettit et al., 1997), to create an "all-optical" approach to neural circuit interrogation. Fifth, by using imaging, the experimenter can precisely determine the relative spatial location of groups of cells, which is particularly crucial since the distance between neurons has been shown to play a role in their connectivity and function (Goncalves et al., 2013). Finally, these methods allow for long-term

chronic imaging over a period of months, allowing for the examination of how cells in a neural network change as an animal develops and learns (Andermann et al., 2010).

Rationale for the thesis research

Calcium imaging is increasingly popular in neuroscience, as evidenced by how just as many publications for calcium imaging in neurons have appeared in PubMed in the last 5 years as in the previous four decades. This trend is likely to continue as the availability of drastically improved GCaMP calcium sensors (Akerboom et al., 2013, Chen et al., 2013), transgenic mice expressing these genetically encoded calcium indicators (Dana et al., 2014, Sato et al., 2015), and more affordable commercial two-photon microscopes and do-it-yourself miniaturized head-mounted miniscopes (Helmchen et al., 2001, Aharoni et al., 2019) are making it increasingly easier and cheaper for mainstream scientists to adopt these techniques.

Unfortunately, analyzing the rich data generated by these methods can be challenging and overwhelming. Motion correction is inherently difficult with a dynamic fluorescent signals, as traditional motion correction algorithms (for non-dynamic signals) may interpret a fluorescence change as movement, and when attempting to correct for it, often introduce artifacts. As more powerful imaging leads to larger data sets, manual motion correction and segmentation of the images into distinct regions of interest (ROI) becomes unfeasible. Manual ROI selection can also introduce human error, favoring more active ROIs. It also becomes difficult to distinguish and detangle overlapping ROIs. Furthermore, many analysis methods rely entirely on the calculation of a change in the fluorescence signal ($\Delta F/F$), without directly correlating it to a biological process.

Scientists who routinely use calcium imaging have had to develop their own custom code (usually in MATLAB) to analyze their data, but because data is acquired differently in different laboratories, it has been difficult for others to incorporate these customized and poorly annotated routines. In the past, there was also a certain degree of unwillingness by some scientists to share their custom-written code or provide well-documented scripts that others could understand.

In recent years, several more sophisticated algorithms have been developed to address these problems (Vogelstein et al., 2010, Pnevmatikakis et al., 2016), but there has yet to be a unified, simple solution to the analysis of such data, particularly one that can be used by the amateurs and non-aficionados. As a result, mainstream neuroscience laboratories who were willing and able to answer their biological questions with calcium imaging but lacked skills in writing new code or modifying existing code, are still waiting for a user-friendly toolbox. A similar platform, *FreeSurfer*, has been extremely useful to the functional MRI community (Fischl, 2012).

The goal of my Ph.D. thesis was therefore to design an intuitive, easy to use toolbox with familiar-looking graphical user interfaces (GUI) that requires no programming experience. In Chapter 1, I describe a calcium analysis software suite that I developed for the detection, extraction, and deconvolution of fluorescent calcium signals. This toolbox, named EZcalcium, incorporates code previously written by other groups, as well as new functionalities I designed, into a single GUI-based pipeline. I also provide examples of how each of these steps are implemented in different types of calcium imaging data. In Chapter 2, I demonstrate the application of the analysis of calcium imaging combined with synchronized sensory stimuli to discover and characterize sensory

abnormalities in a mouse model of fragile X syndrome. Detailed methods are provided at the end of each chapter.

Chapter 1

EZcalcium: A comprehensive and user-friendly toolbox for analysis of fluorescence calcium signals

BACKGROUND

The ideal solution for calcium imaging analysis would address all the core aspects of analysis: image registration (motion correction), segmentation into distinct regions of interest (ROI), signal extraction (dimension reduction), deconvolution, data exporting, and data plotting. The entire process should be fully automated (e.g., unbiased ROI selection), fast, and compatible with standard desktop or laptop computers. The code should be well-documented with discreet variable and function names that allow users to examine how the code works and to make modifications. The code should also be modular, so that users can implement functions into their existing routines and add their own new functions. Additionally, the code should be wrapped in a set of user-friendly GUIs so that scientists who are not proficient in writing code in MATLAB can quickly and easily learn to work with the interface. This solution should be versatile and be compatible with a variety of microscope file formats, and also account for different acquisition speeds, field of view size, or image resolution. Additionally, it should be adaptable to accommodate yet-to-be-developed dynamic fluorescence indicators. Ideally, the segmentation process should be able to differentiate ROIs of different cell types or cell compartments (e.g., dendrites, spines, axon boutons, astrocytic processes). Such an automated system would also allow for batch processing, such that even older computers can process multi-gigabyte video files in a few hours.

We present our version of such a solution, EZcalcium, an open-source, modular, and adaptable software suite designed for motion correction, ROI detection, signal extraction, and deconvolution of fluorescent calcium imaging data. It has already been successfully implemented in several

published studies (He et al., 2017, Goel et al., 2018, He et al., 2018) and is freely available at Github.

DESCRIPTION OF THE TOOLBOX

Overview

The EZcalcium toolbox is controlled by a set of intuitive and user-friendly graphical user interfaces (GUI). Once configured for a set of similarly-acquired data, preferences can be saved and reused for simple automation of workflow. The toolbox is able to import a variety of imaging data file types (including .tif, .avi, .mat) and supports export of data in both proprietary (.mat, .xlsx) and open file formats (.csv).

EZcalcium contains three main modules: Motion Correction, ROI Detection, and ROI Refinement. An algorithm for how a typical data file is processed through this workflow is shown in **Fig. 1**. In the sections below we describe what these three modules achieve and then illustrate the results with specific examples from in vivo calcium imaging experiments done in mice and Drosophila, with 2-photon microscopy or miniscopes. A more detailed step-by-step walkthrough tutorial is presented in the section entitled **Procedures.** The *Motion Correction* module consists of a non-rigid method of template matching, background subtraction, and the ability to export corrected videos with lossless compression. The *ROI Detection* module, built off of the *CaImAn* toolbox (Giovannucci et al., 2019), includes automated ROI detection, signal extraction, and deconvolution of fluorescence calcium signals. The *ROI Refinement* module enables the user to sort and view

ROIs, manually exclude ROIs, and use automated and customized ROI exclusion criteria, including spatial and activity-dependent metrics.

Figure 1

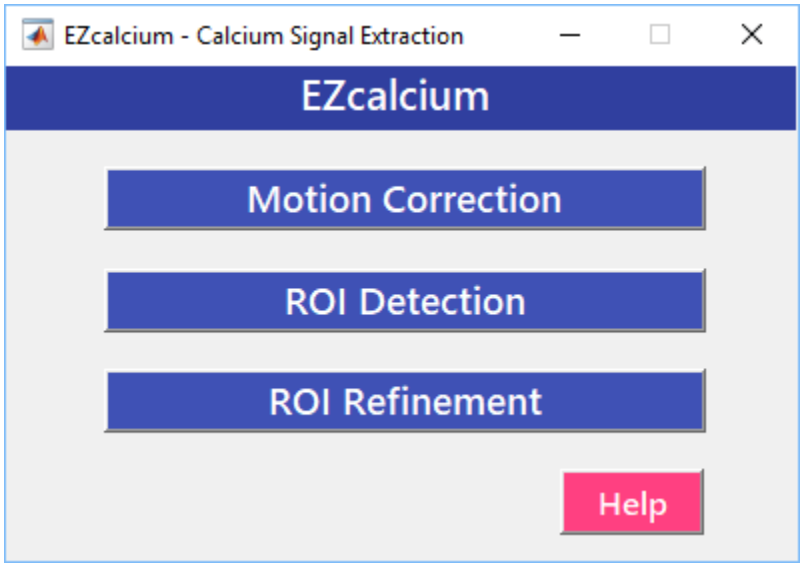

Figure 1. EZcalcium control GUI. Each module of the toolbox is called by clicking on its respective button. *Help* buttons are located throughout the toolbox to provide documentation and resources to the user.

Batch processing is supported in the most resource-intensive modules (Motion Correction, ROI Detection) and allows for a large number of files to be sequentially loaded, processed, and saved. This feature is ideal for processing large data sets (>4 GB) that would best be processed overnight or on a dedicated analysis machine. In the event of a system 'crash' or shutdown, as can occur during an automatic operating system update, progress is automatically saved at the end of each successful file processing and can be resumed from the start of the previous incomplete attempt.

The MATLAB source code is freely available for all modules so that users may modify and adapt the code as they see fit. It is well-documented within the code itself for easy understanding and to facilitate modification. The code is designed to be modular and adaptable for use with dynamic fluorescence data obtained from a wide variety of imaging systems, including miniscopes, and should easily translate to other types of dynamic fluorescence imaging, such as voltage sensors and indicators of neurotransmitter release. Standalone, compiled executable files are also provided for users, which allows the toolbox to be used on different systems without the need of a MATLAB license or any programming experience. Standalone executables are ideal when using a computer cluster to process very large data sets, such as those acquired through prolonged continuous calcium imaging.

We have tested the EZcalcium toolbox on calcium imaging data collected with *in vivo* two-photon microscopy in neurons of primary visual cortex expressing GCaMP6s, in the visual system of Drosophila larvae, in boutons of thalamocortical axons in layer 4 in barrel cortex, and in cortical astrocytes, as well as with miniscopes in the CA1 region of the hippocampal formation.

Motion Correction

Motion correction of calcium imaging data is inherently difficult due to the nature of dynamic fluorescence imaging and is further complicated by movement artifacts associated with imaging in the living animal. The latter problem creates primarily translational drift in x and y directions and is relatively easy to correct. In contrast, the fluorescence signal intensity of the profile being imaged (cell body, axon bouton) can fluctuate depending on whether the element is active or not, which simple static registration algorithms may mistake for actual translation in the x-y dimension. A number of different strategies have been introduced for image registration based on template matching (Greenberg and Kerr, 2009, Mineault et al., 2016). Hence, a variety of template matching options are provided in EZcalcium for the user to implement motion correction. Since the kinetics of current genetically encoded calcium indicators (GCaMP, etc.) are relatively slow compared to commonly-used acquisition speeds (typically ~8-30 frames per second), sequential frame matching is particularly useful as a first-pass motion correction approach for calcium imaging, as any given image frame is fairly similar to the previous frame. Multiple iterations of template-matching can be performed under EZcalcium. For GCaMP indicators, the recommended approach is to start with one round of sequential frame template matching, followed by multiple (3-5) iterations of matching to a mean image template generated using all the frames in the video (**Suppl. Fig. S1a**). We find that this registration procedure provides excellent results for data collected from awake behaving mice or Drosophila with 2-photon microscopy (**Fig. 2a-d**), as well as data from freely moving mice obtained with miniscopes (**Fig. 2e, f**).

A minimal form of background subtraction is included as an option during Motion Correction (**Suppl. Fig. S1b**). This removes the minimum value from each pixel and does not alter signal strength. It can be used to aid in manual refinement by eye to test and verify settings for an automated workflow. This is especially useful in high-background imaging, such as miniscopes (**Fig. 2e, f**). The output of Motion Correction is a corrected video of the user's desired file type. Lossless compression options are available that reduce file size without losing any data. Of course, it is not strictly necessary to perform the Motion Correction step if the videos do not exhibit motion artifacts (e.g., calcium imaging in brain slices or anesthetized mice).

Figure 2

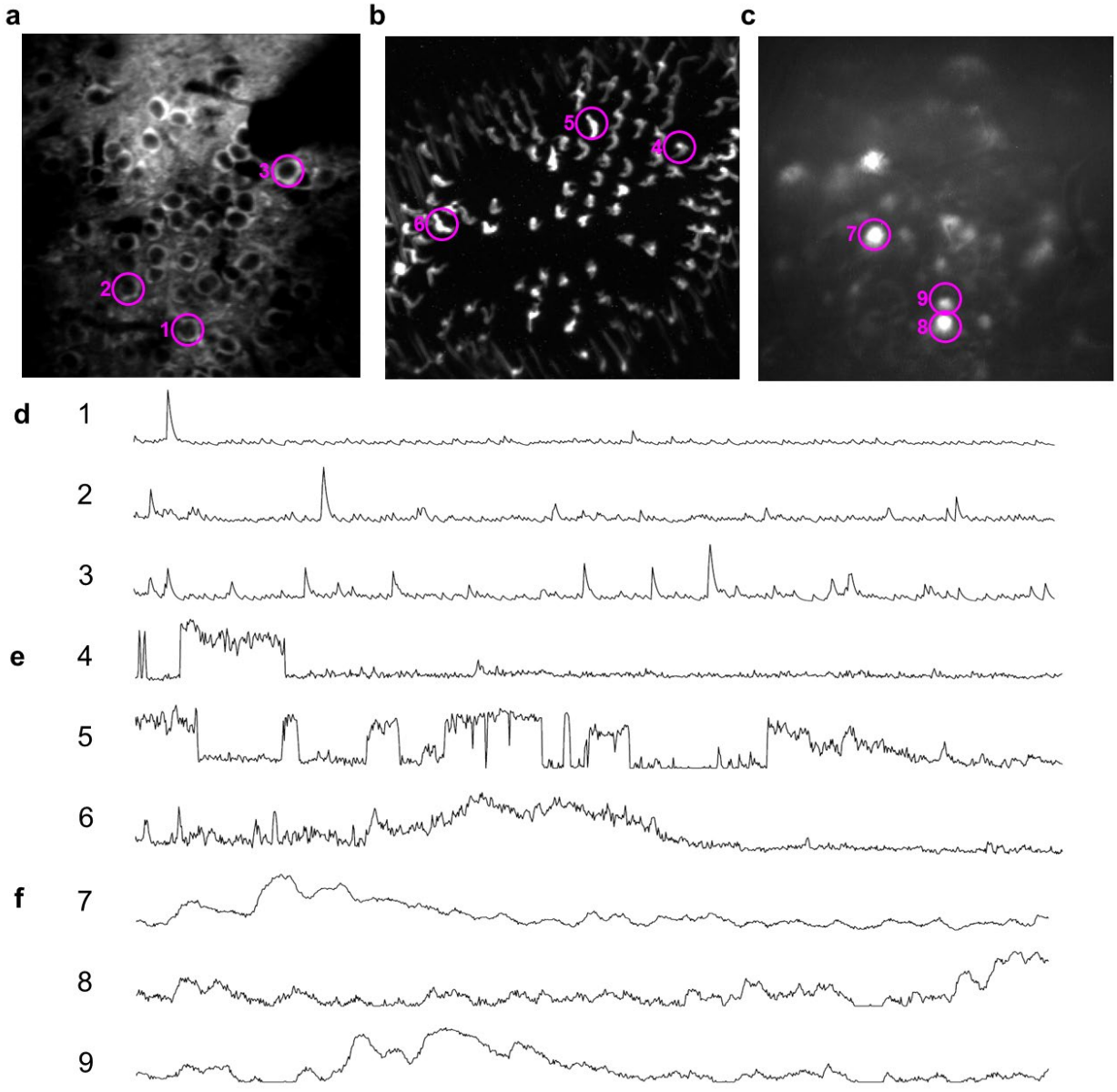

Figure 2: Motion correction and extracted traces of assorted animal models

(a) Standard deviation projection of motion corrected mouse primary somatosensory cortex imaging

(b) Extracted ΔF/F traces from mouse primary somatosensory cortex

(c) Standard deviation projection of motion corrected *Drosophila melanogaster* imaging

(d) Extracted ΔF/F traces from *Drosophila melanogaster* imaging

(e) Standard deviation projection of motion corrected CA1 miniscope imaging

(f) Extracted ΔF/F traces from mouse CA1 miniscope imaging

ROI Detection

After movies are aligned, the next step in processing the data is to segment the image into the desired regions of interest (ROI). Automation of ROI selection can diminish the effects of bias and significantly reduce the time required to process large data sets. Our GUI-based ROI Detection module incorporates select aspects of the *CaImAn* toolbox (Giovannucci et al., 2019). Although it can be fully automated, ROI Detection in EZcalcium also allows for manual refinement of initially-estimated ROI centers as an optional step for adding or removing ROIs by hand. When manual initialization is included, batch processing is fully automated. ROI Detection is based on using both temporal and spatial correlations to identify nearby pixels that exhibit similar changes in fluorescence intensity at the same time. It initializes by estimating activity using power spectral density or sparse non-negative matrix factorization (Maruyama et al., 2014). Different ROI search methods (ellipse, dilate, etc.) are available in EZcalcium, depending on what was imaged; some are better suited to detect somata, while others are better for dendritic spines (Pnevmatikakis et al., 2016). Similarly, the user can estimate the ROI size and number, to optimize the results. After a processing a single video, the user will be provided measurements of actual ROI size and number, which can be used to improve the performance of further ROI detection.

Multiple temporal iterations are used to improve accuracy and to detect ROIs of complex shapes (which is relevant for irregular profiles in Drosophila and axonal boutons; **Suppl. Fig. S2a, b**). Overlapping components with similar activity can also be combined post-hoc to form single functional ROIs.

The ROI Detection module also generates data regarding the fluorescence intensity over time for each ROI through the following operations: Background activity is subtracted, neuropil signals are removed, and ΔF/F data is extracted for each ROI (Pnevmatikakis et al., 2016). These signals can also be deconvolved into firing probability rates using various deconvolution algorithms (Vogelstein et al., 2010). The modularity of the code allows for novel deconvolution algorithms to be implemented by the user, including calibrated deconvolution using simultaneous electrophysiological recordings (Golshani et al., 2009, Chen et al., 2013). In its present form EZcalcium only provides a 'low hanging fruit' level of analysis of calcium signals. Nevertheless, additional features can be added as other modules depending on the specific needs of the user. For example, we have developed distinct modules suitable for analysis of calcium data from visual cortex (e.g., percent of ROIs that are orientation selective, tuning width, etc.) and barrel cortex (percent of ROIs that are time-locked to whisker stimulation, adaptation index, population coupling).

ROI Refinement

The process ROI Detection works best when searching for too many ROIs rather than too few. As such, an additional step of ROI exclusion is necessary. ROI Refinement automates ROI exclusion using user-defined heuristics to judge ROIs for validity. By automating this process, operator biases can be minimized. ROI Refinement criteria include characteristics of ROI morphology and activity. The ROI Refinement GUI also allows the user to readily view the characteristics of all detected ROIs, including a visual map of the ROI's location, the shape of the isolated ROI, and the extracted fluorescence traces in raw, ΔF/F, and deconvolved formats (**Fig. 3**). This helps in

defining what criteria should be used for excluding ROIs from further analysis. It can also be used to manually include or exclude ROIs. After ROI Refinement is completed, data can be exported into proprietary (.mat, .xlsx) or open file formats (.csv). Additionally, ROI refinement can be re-performed in order to select different subsets of cells (such as those of a particular level of Kurtosis (Ringach and Malone, 2007)) and to save the data separately.

Figure 3

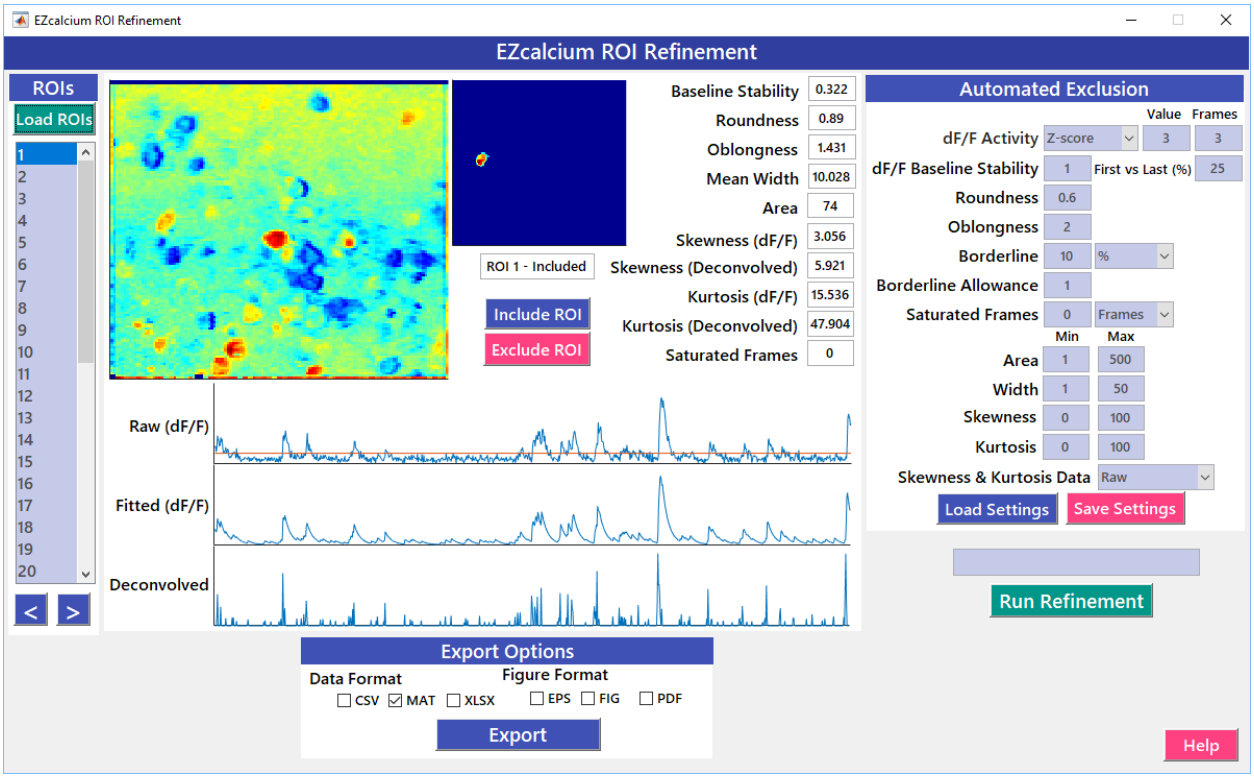

Figure 3. ROI Refinement GUI. *ROI Refinement* is the final step of the EZcalcium workflow and consists of automatically or manually excluding ROIs based on shape and activity. Following refinement, data can be exported in a variety of formats. An example ROI is shown following refinement.

Computational Performance

Over the next decade or two, there will be increased pressure to record from increasingly larger numbers of neurons at faster temporal resolution in behaving mice, over longer recording times, which will inevitably lead to a geometric increase in the size of the files to be processed. From a computer performance standpoint, ROI Detection and Motion Correction are the two most resource-intensive modules. The amount of time required for these steps expands non-linearly with file size. As such, image acquisition capability threatens to outpace image processing capability. Graphics processing unit (GPU)-powered analysis would need to be implemented by taking advantage of the modular nature of the code and inserting the appropriate algorithms. This would potentially allow multiple frames of an imaging file to be simultaneously processed, increasing the rate of video analysis. However, this capability is not included in this version of EZcalcium as it would require specific hardware, greatly limiting the number of computers that are capable of using the toolbox. As the code currently stands, to process video files 10 GB or larger, a dedicated processing computer with a fast CPU, a large amount of RAM, and a solid-state working hard drive is recommended. Using MATLAB's capabilities to distribute a workload to an ethernet-connected computing cluster would be another way to rapidly increasing the processing capabilities of the code. The simplest way to process a large number of videos is already built-in: install the toolbox on multiple computers without the need for a MATLAB license and batch-process different videos on each computer.

RESULTS

The included file *EZcalcium_demo.tif* will be used as a practice case study and an example for the user to verify that all steps are being performed correctly. This video was recorded from neurons in Layer 2/3 of adult mouse primary visual cortex (V1) expressing GCaMP6s (4 weeks after injection of rAAV-syn-GCaMP6s) in a 2-month-old mouse at ~15 Hz using a custom built 2-photon microscope. This was an awake head-fixed mouse that was allowed to run on a polystyrene ball floating on an air cushion, while passively viewing sinusoidal gratings drifting in different directions (Goel et al., 2018). The video was down-sampled spatially and temporally to a relatively low resolution (128 x 128 pixels, 1,000 frames, 7.81 Hz) to demonstrate the ability to extract data from limited videos and to ensure that the toolbox will run properly with minimal hardware requirements. The settings files for all steps are also included as part of the demo. *EZcalcium_demo_motcor.mat* is used for Motion Correction, *EZcalcium_demo_detect.mat* for ROI Detection, and *EZcalcium_demo_refine.mat* for ROI Refinement.

Motion Correction (**Figure 4**) was performed using three iterations of an all-frames *Mean* template with *Minimal* background subtraction and LZW compression. The video was processed as a single block due to the initial stability of imaging. Although the original video file was quite stable, cell somata are more clearly-defined in the motion-corrected, background-subtracted video. By increasing the stability of imaging, automated ROI detection will be more accurate, and the signal-to-noise ratio of extracted traces will most likely improve.

Figure 4

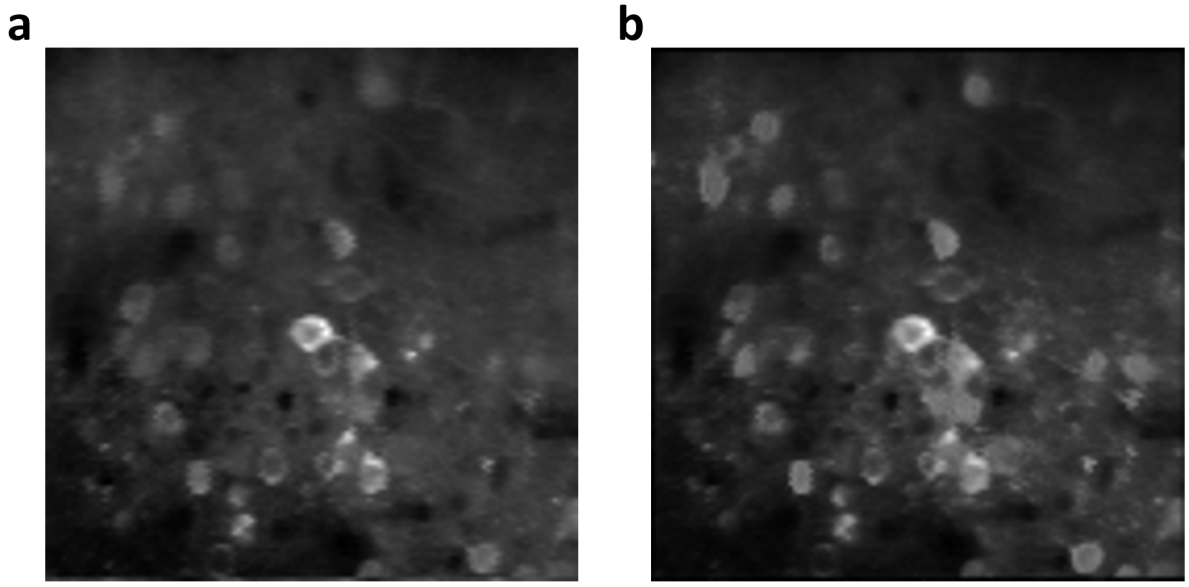

Figure 4. Comparison of images following *Motion Correction*. Standard deviation Z-projection of *EZcalcium_demo.tif* before (**a**) and after (**b**) motion correction and background subtraction. Cell soma are visibly more apparent following *Motion Correction*.

ROI Detection (**Figure 5**) was then performed on the motion-corrected video using *Greedy* Initialization, *Ellipse* search method, *SPGL1 Constrained foopsi* deconvolution, and *Decay* autoregression. 50 components with a component width of 6 were used to locate ROIs of the appropriate size. Manipulating the component width had the largest impact on accurate ROI tracing. Although manual initialization refinement was selected to be performed, no ROIs were added or removed following initialization. Extracted dF/F traces exhibit the bursting activity patterns typically seen in layer 2/3 pyramidal cells in mouse V1. Additionally, the timing of elevated dF/F generally correlated with the presentation of visual stimuli.

Figure 5

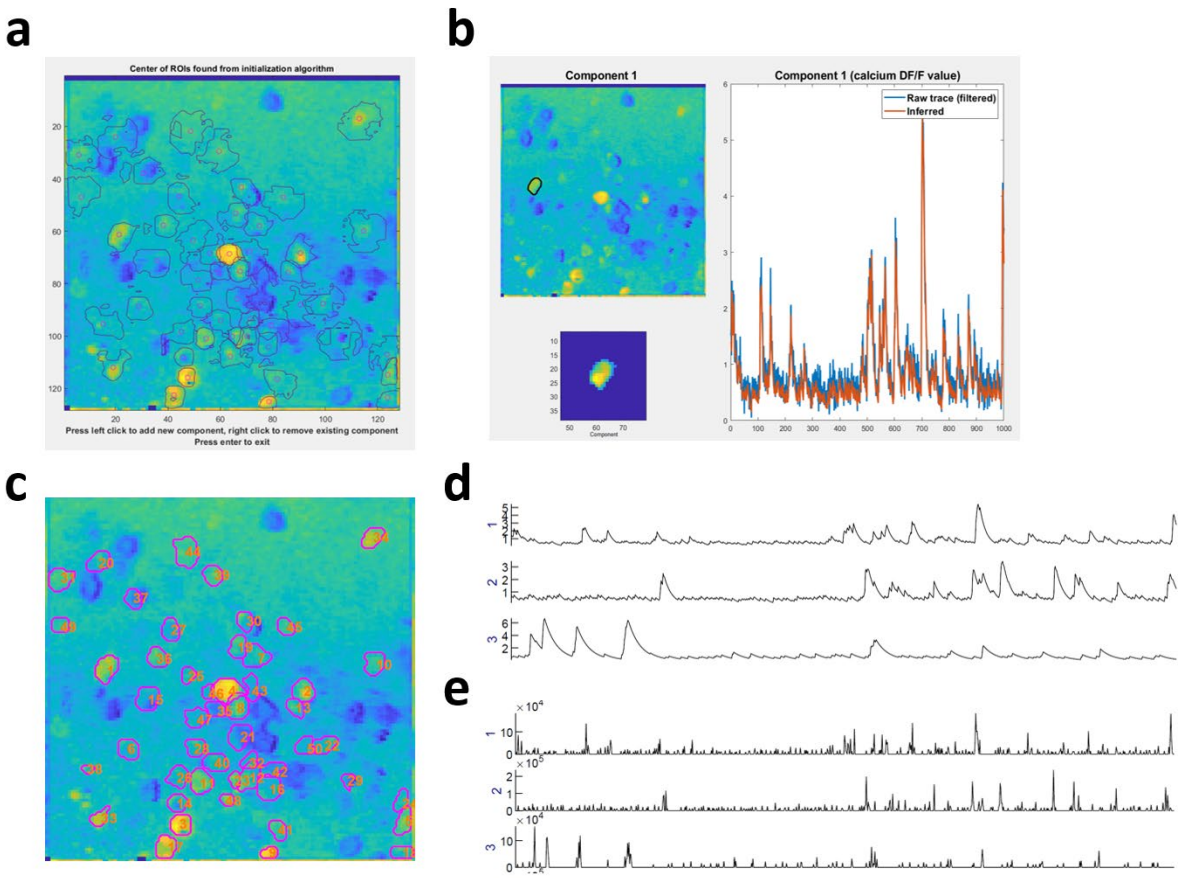

Figure 5. Automated *ROI Detection* in mouse primary visual cortex. *ROI Detection* initialization refinement (**a**), component view (**b**), and complete map of identified ROIs (**c**) identified from low-resolution imaging of mouse primary visual cortex expression GCaMP6s. Extracted dF/F traces (**d**) and deconvolved calcium signals (**e**) are shown from the first three ROIs.

ROI Refinement (**Figure 6**) was performed using the provided *EZcalcium_demo_refine.mat* settings file. As in previous experiments examining dF/F activity in mouse V1, a criteria of activity levels exceeding a median absolute deviation of 3 for a minimum of 4 consecutive frames was included. Overall, automated ROI Refinement selected 38 out of 50 ROIs for inclusion. The refinement criteria generally favored rounder ROIs with clear sustained signals above baseline.

Figure 6

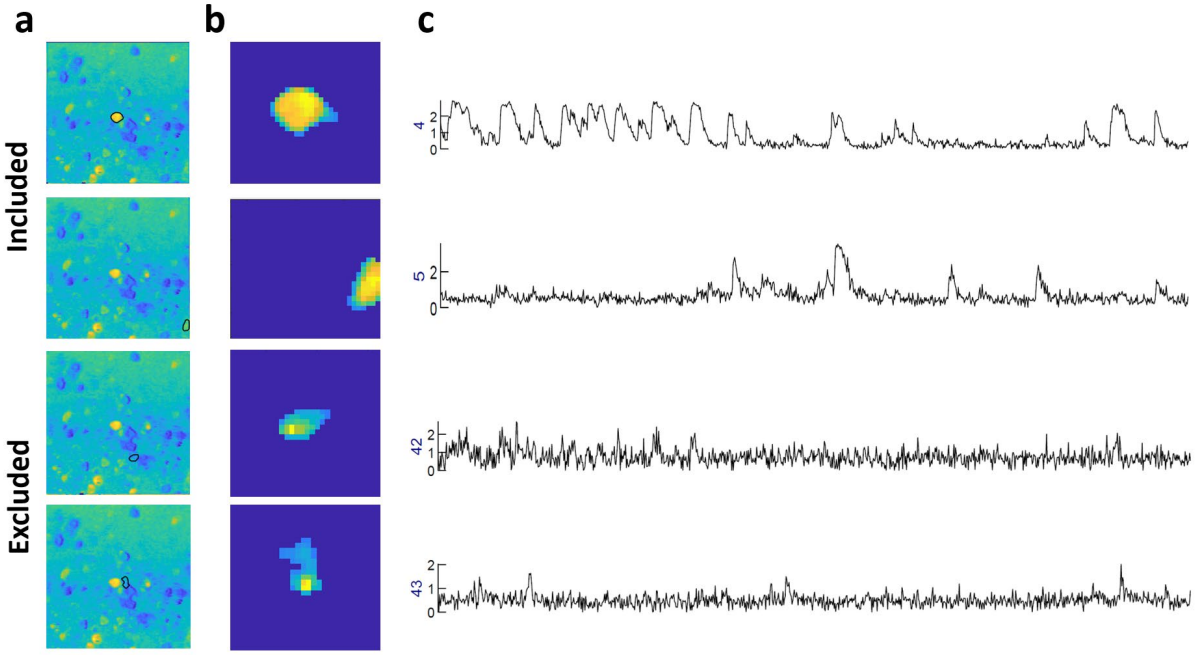

Figure 6. ROIs sorted by automated *ROI Refinement*. Example locations (**a**), isolated ROIs (**b**), and raw dF/F activity traces (**c**) and isolated shapes of included (top two sets) and excluded ROIs (bottom two sets) following *ROI Refinement*. Included ROIs generally have rounder shapes and sustained bursts of activity above baseline fluorescence.

MATERIALS AND METHODS

Equipment

A MATLAB license or programming experience is not required to run the toolbox as a standalone executable file; however, the EZcalcium executable is currently only available for Windows operating systems. We recommend 64-bit MATLAB R2018a (or newer MATLAB) on any operating system for using the EZcalcium toolbox within MATLAB. The toolbox was finalized and tested heavily in R2018a (9.4) and is likely to be the most compatible without modification in that environment. A 64-bit version of MATLAB running on a 64-bit computer is required to process files over 800 MB. The following MATLAB toolboxes are also required when running the source scripts: Signal Processing, Statistics, and Parallel Computing. The amount of available system RAM necessary for a system depends on the size of the data being processed. Ideally, the amount of system RAM should be at least 3X the file size of raw, uncompressed data. Motion Correction is the most RAM-intensive step of the process and significant slowdowns may occur if the necessary RAM is not available. CPU requirements for the toolbox are minimal, but processing is vastly improved with multiple cores. The toolbox also runs faster when the data to be analyzed is located on a fast, solid-state hard drive, since large amounts of data must be read and, in the case of Motion Correction, written.

Software Setup

EZcalcium is freely available to be downloaded from the Portera-Cailliau Lab Github. For running the executable version, a MATLAB 2018a runtime or installed version of MATLAB is required. MATLAB runtimes are available for free on the MATLAB website:

https://www.mathworks.com/products/compiler/matlab-runtime.html. When running the executable, a command window should be the first thing that loads. It may take several minutes for the first GUI to load. To run the toolbox source code, first add the toolbox folder to the MATLAB path directory. Type the command EZcalcium. A GUI will load that can run all the individual modules **(Figure 1)**. When working in Windows, data saved to directories listed under C:\Users, C:\Program Files, and the directory in which MATLAB is installed are often protected against writing and deletion. Therefore, in order to process and generate data, it is recommended to use imaging files saved outside of C:\Users, C:\Program Files, and the directory in which MATLAB is installed. Failure to do so may result in an error stating "You do not have write permission."

PROCEDURES

Below are step-by-step instructions for using the three modules of EZcalcium toolbox.

Motion Correction

1) From the initial GUI, click on the box titled *Motion Correction* to load the Motion Correction GUI **(Figure 7)**

Figure 7

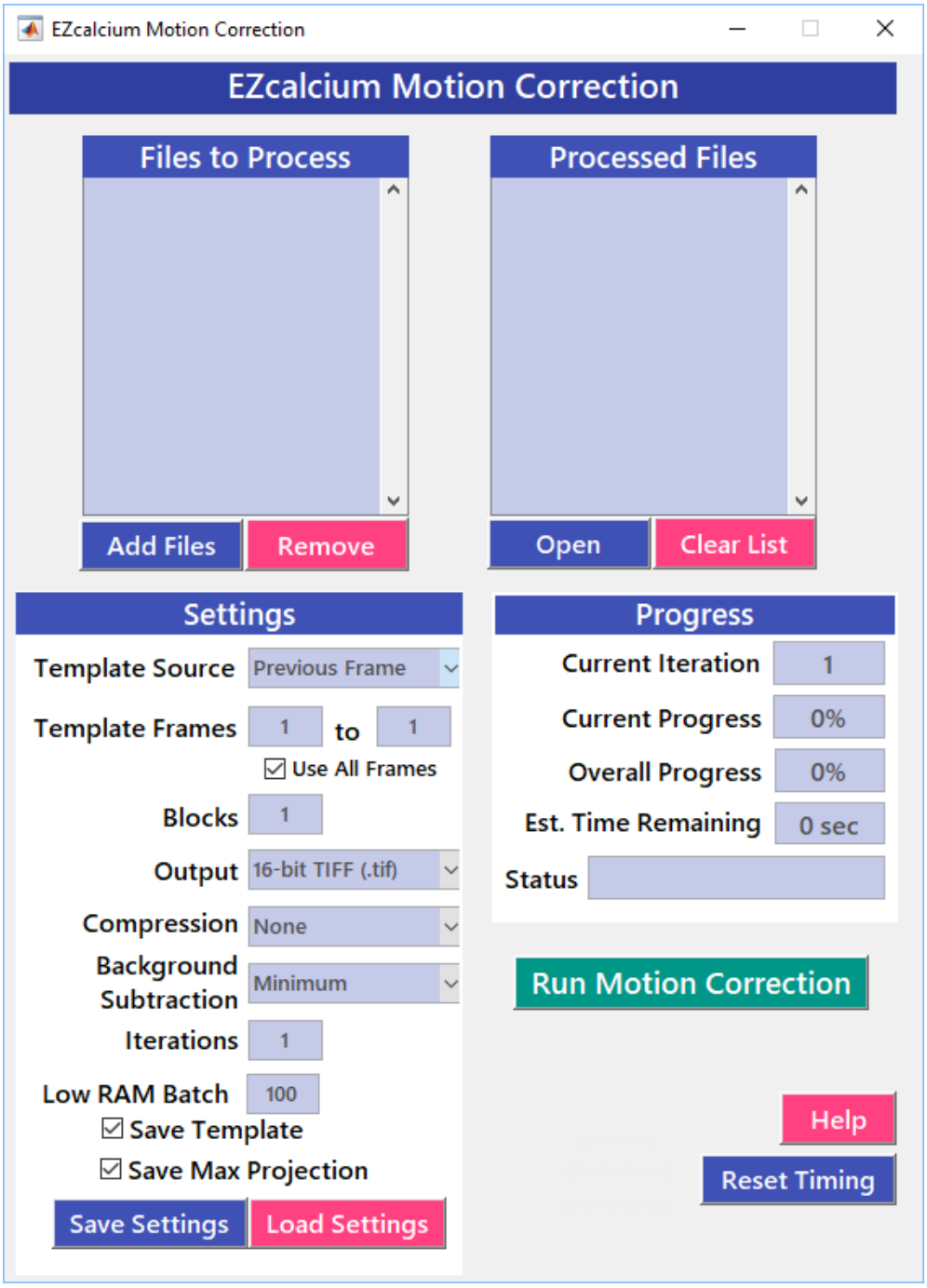
EZcalcium Motion Correction
EZcalcium Motion Correction
Files to Process
Processed Files
Add Files
Remove
Open
Clear List
Settings
Template Source
Previous Frame
Template Frames
1
to
1
Use All Frames
Blocks
1
Output
16-bit TIFF (.tif)
Compression
None
Background Subtraction
Minimum
Iterations
1
Low RAM Batch
100
Save Template
Save Max Projection
Save Settings
Load Settings
Progress
Current Iteration
1
Current Progress
0%
Overall Progress
0%
Est. Time Remaining
0 sec
Status
Run Motion Correction
Help
Reset Timing

Figure 7. Motion Correction GUI. The *Motion Correction* module can be used for correcting lateral motion during imaging, removing static background information, and compressing videos without losing any data.

2) In the Motion Correction GUI, click the Load button to choose any number of videos you would like to load. You can drag a box or use the select or *shift* key to select multiple files with the mouse. If you close the file select window and decide to add more files later (e.g., from a separate folder), they will appear at the bottom of the list. If you accidentally try to add the same file multiple times, it will not be added to the list again and an error will display. Compatible file types include multipage 8- or 16-bit .tif, .avi, and .mat in which the largest variable in the .mat workspace is a three-dimensional matrix of *xyz* dimensions. Files used need to be single-channel images. .tif files greater than 4 GB need to be in an uncompressed format. If your data is of an incompatible file type, it can likely be converted to .tif or .avi with free software such as ImageJ, available at https://imagej.nih.gov/ij/

3) To remove a file that has been added to the *Files to Process* list, select the file with the mouse and click the *Remove* button.

4) Choose a template source from the list *Template Source.* Choosing *Previous Frame* will align each frame, starting with the second frame, to its previous frame. *Mean* and *Median* calculates the mean and median intensity value for each pixel, respectively. *Max Projection* creates a projection of the highest intensity value of each pixel. *Brightest Frame* detects the frame with the overall highest pixel intensity

5) Choose the number of frames from which to create the template under *Template Frames.* If a large section of the video is stable and has a representative amount of fluorescence signal, but

other sections exhibit a lot more motion artifact, it may be useful to restrict *Template Frames* to the stable frames of the video. Checking the box *Use All Frames* will automatically detect and use all the frames in any given video and ignore the input values.

6) Set the number of *Blocks*, which refers to the number of blocks (spread vertically) that the image will be divided into prior to alignment. To register the image as a single block, enter a *Blocks* value of 1. Generally, using a larger number of blocks processes faster than using fewer blocks, due to the ease of aligning several smaller blocks instead of larger more complex images. However, it may also introduce artifacts on otherwise steady videos if blocks are too numerous. For example, a *Blocks* value of 8 for a 256x128 will break down into a total of 64 32x16 blocks in an 8x8 configuration (**Suppl. Fig 1c**). *A* recommended value for *Blocks* would be less than the square root of the number of pixel rows (video height).

7) Select a format for the corrected video to be saved under *Output.* 8-bit or 16-bit should be chosen to match the bit depth of the image acquisition. Although .mat files will load quickly for ROI selection, they are not viewable in ImageJ and other software packages. In EZcalcium, saving as a .mat is currently the only way to save a compressed version of .tif files over 4 GB.

8) Lossless compression options for saving .tif files are available under *Compression.* These can reduce file size without losing any data but will likely take longer to save. These do not apply to .mat or .avi files. *Deflate* generally results in the smallest file size when saving 16-bit .tiff files smaller than 4 GB. *Packbits* is usually the fastest form of compression but it may not reduce file size as much as other methods. If the user selects *None*, this will result in no compression and will save in the fastest time, although this will also result in larger file sizes. For EZcalcium, *None* must be selected for saving .tif files over 4 GB.

9) *Background Subtraction* will remove elements of the images determined to be related to background changes in fluorescence intensity. The choice of *Minimum* removes the minimum value of each pixel from the pixel. This is useful for removing constant sources of brightness, such as bleed-through fluorescence, without impacting changes in imaged activity.

10) *Iterations* refers to the number of repeated times the user wishes to perform motion correction. For a *Template Source* such as *Mean*, multiple iterations are useful so that the mean image projection used for the template will change with each iteration and result in improved motion correction. *Iterations* should generally be less than 7.

11) The *Save Template* option saves the template that was generated and used for alignment, for further reference. *Save Max Projection* saves a maximum intensity projection of all frames, no matter what template source was used.

12) The *Save Settings* button allows the user to save all settings under a specific name of your choosing. Settings are saved as .mat files. These include all settings in the *Settings* section as well as timing data that records how long it took to go through the main steps of the previous five video alignments.

13) The *Load Settings* button allows one to load all saved settings in future sessions.

14) Once all settings are configured, click the *Run Motion Correction* button. Immediately after attempting to start motion correction, and autosave file is automatically generated and updated as progress continues. This will automatically load the last used settings when the application is next used. Progress of motion correction will display the current iteration of motion correction, the current progress of the current iteration, and the overall progress of the all the files listed in the *Files to Process* list. *Est. Time Remaining* displays the estimated time remaining for all the files to

be motion corrected. Time estimates may not be updated under when loading or saving .mat files or when loading uncompressed .tif files.

15) After motion correction is completed, the new file generated will be added to the bottom of the *Processed Files* list. Original files will not be overwritten. A new file will be created with *_mcor* and the number of iterations appended to the filename.

16) The *Open* button will open the selected file in the default program set by the operating system.

17) *Clear List* clears the entire list of *Processed Files*.

18) The *Reset Timing* button can be used when creating a new configuration or working with files of a different size. It will reset all timing information on how long individual steps typically take that are used for calculating *Est. Time Remaining*. After running motion correction five times on a new configuration, *Est. Time Remaining* should be the most accurate. In the event that stored timing information is corrupted and *Est. Time Remaining* displays as "NaN", click the *Reset Timing* button to clear it.

ROI Detection

1) From the initial GUI, click on the icon titled *Automated ROI Detection* to load the *ROI Detection* GUI **(Fig. 8)**.

Figure 8

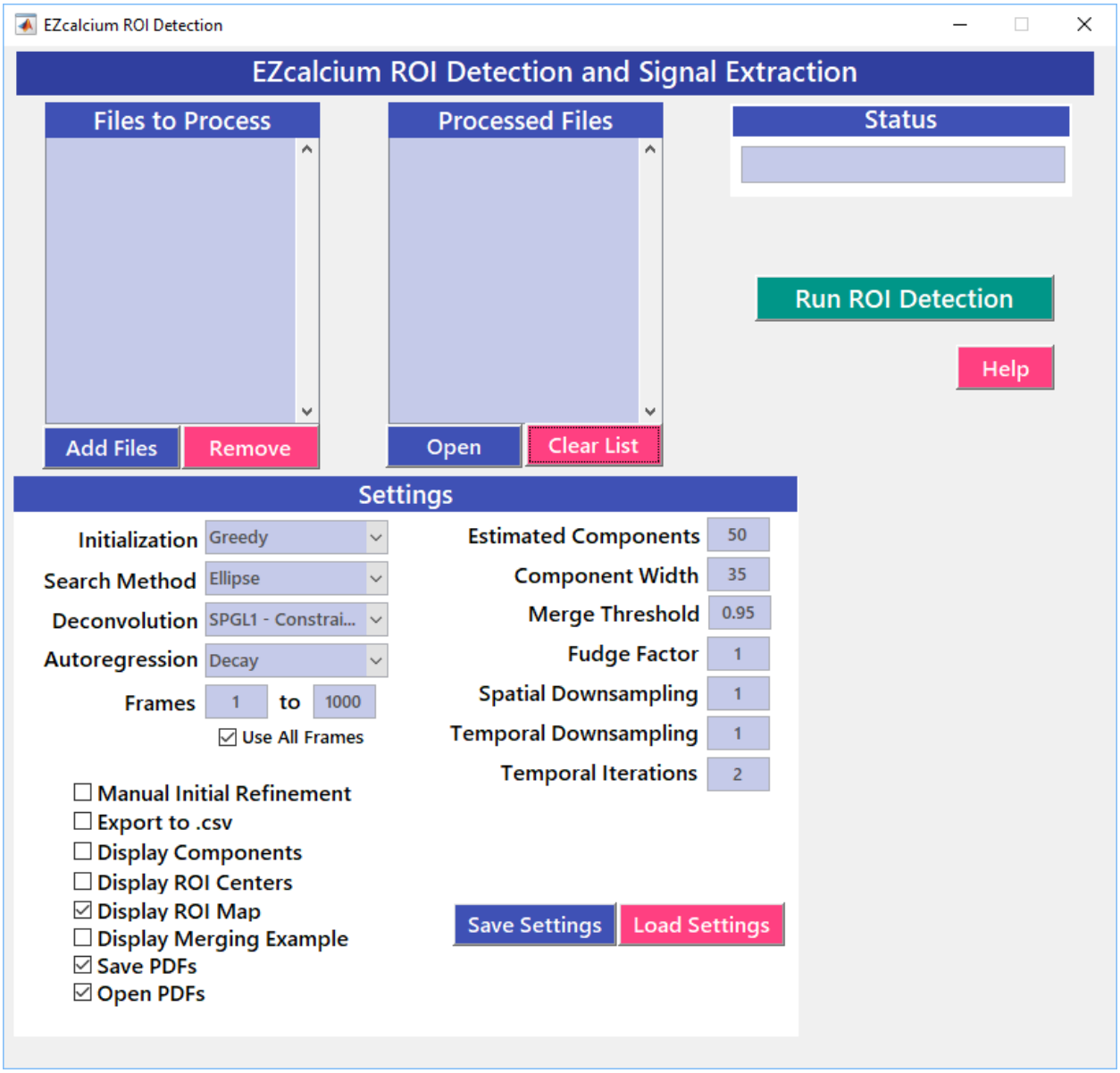

Figure 8. ROI Detection GUI. The automated *ROI Detection* module can be used to detect ROIs from batches of videos and minimize the impact human biases in ROI tracing. Manual initial refinement can also be performed to select any ROIs that may be missed by the automated detection process.

2) In the *Automated ROI Detection* GUI, click the *Load* button to choose any number of videos you would like to load. Compatible file types include multipage .tif, .avi, and .mat in which the largest variable in the .mat workspace is a 3-D matrix of xyz dimensions. One can drag a box or use the select or shift key to select multiple files with the mouse. The user closes the file select window and decides to add more files later, such as from a separate folder, the files will appear at the bottom of the list. If the user accidentally tries to add the same file multiple times, it will not be added to the list again and an error will display. File type requirements for ROI Detection are similar to that of Motion Correction. When troubleshooting and testing motion correction for the first time, it is advisable to start with correcting a single file and testing the settings.

3) To remove a file that has been added to the *Files to Process* list, select the file with the mouse and click the *Remove* button.

4) *Initialization* methods for providing an initial estimate of spatial and temporal components: *Greedy* is recommended for videos of neuronal somata. It relies heavily on spatial components and generally runs much faster; *Sparse NMF* is recommended for more complex structures, such as dendrites, dendritic spines, or axons.

5) *Search Method* determines the spatial components (location) of ROIs: *Ellipse* assumes components have an ellipsoid shape, such as for neuronal somata; *Dilate* can be used with either ellipsoid or non-ellipsoid ROIs, but generally takes longer.

6) *Deconvolution* determines the method for translating activity-induced changes in the fluorescence intensity of the indicator into approximate firing rates. If you are imaging an organism that does not produce action potentials, set this to the fastest setting available. Noise-constrained deconvolution methods include *SPGL1 - Constrained foopsi* and *CVX - Constrained*

foopsi. Both are also available through https://github.com/epnev/constrained-foopsi. *SPGL1* - *Constrained foopsi* works well even with medium-to-low signal-to-noise traces. *CVX* - *Constrained foopsi* requires CVX and is not available in the standalone version of EZcalcium. It is typically the fastest method of deconvolution when working with high signal-to-noise traces. It is available at http://cvxr.com/cvx/doc/install.html. *MCMC* is a fully-Bayesian deconvolution method that is computationally-intensive and is recommended when higher precision is required. *MCEM* alternates between the listed *Constrained foopsi* deconvolution and *MCMC* to update time constants. It is significantly faster than *MCMC* alone and is generally recommended when deconvolving calcium signals from cell somata.

7) *Autoregression* is used to estimate the calcium indicator kinetics. *Rise and Decay* estimates both the rise and decay kinetics of the calcium indicator and incorporates them when extracting fluorescence traces and deconvolving the signal. Due to the difficulty in detecting fast rise times, using *Rise and Decay* may result in overfit data if the imaging was performed at low temporal resolution (<16 Hz). *Decay* estimates just the decay kinetics of the calcium indicator and is the recommended setting for lower temporal resolution imaging. *No Dynamics* will produce only raw traces and will not perform deconvolution.

8) Choose the number of frames to analyze under *Frames*. Checking the box *Use All Frames* will automatically detect and use all the frames in any given video and ignore the inputted values

9) *Manual Initial Refinement* adds an additional step following initialization to manually add or remove ROIs. ROIs can also be removed in the step *ROI Refinement*. To fully automate the process, it is recommended to optimize your settings to slightly overestimate the number of ROIs and then remove erroneous ROIs later. This step is included as an option for particularly

troublesome files and for those who prefer semi-automated ROI selection. Initial spatial components will be displayed in a new figure. The center of estimates in ROIs is highlighted with a magenta circle, surrounded by the boundary of the ROI. To manually add an ROI, left click with the mouse where you want to add the center of an ROI. The boundary of the ROI will be automatically computed and drawn. To manually remove an ROI, right click on any ROI center. Hit the enter key to continue ROI detection.

10) Choose how you would prefer to export the data. *Save to .mat* exports to a .mat that is necessary for the final step, *ROI Refinement. Output to .csv* exports the same data as *Save to .mat,* but to a .csv file that can be opened in a variety of programs outside of MATLAB.

11) Choose which additional figures you want generated. When batch processing many files, it is not recommended to use these. *Display Contours* shows extracted raw fluorescence data, the inferred trace generated, and the ROI shape and location. *Display ROI Centers* generates a map showing the centers of all ROIs following initialization *Display Merging Example* shows an example of how several components were merged to form a single ROI. This is useful when optimizing *Merge Threshold* and *Component Width. Display ROI Map* generates a map with all the ROI boundaries, each labeled with the same ROI number as was used in the data.

12) *Estimated Components* is the estimated maximum number of components in the field of view. Multiple components may make up a single ROI, so set this value based on your method of ROI detection. This must be set to a minimum value of 1. If you want to perform fully manual ROI selection, set *Estimated Components* to 1 and check the box to enable *Manual Initial Refinement*. When the manual refinement step starts, delete the initial automatically detected ROI.

If no components are determined to be similar enough to be merged, the most likely result is that the number set for *Estimated Components* is the number that will be initially detected.

13) *Merge Threshold* is the threshold at which two components will be merged into a single ROI. Components that share a correlation coefficient above *Merge Threshold* will be merged into a single ROI.

14) *Component Width* is the estimated width, in pixels, of your components. If you have a simple ROI shape, such as a cell soma, you can use the width of the entire ROI as your component width.

15) *Fudge Factor* is useful for estimating time constants of very noisy data, in particular those with low temporal resolution (slow frame rate). The value indicates a multiplicative bias correction for time constants of each ROI during deconvolution. *Fudge Factor* should generally be set to 0.95-1. A value of 1 indicates that no bias correction will be performed.

16) *Spatial Downsampling* will downsample the spatial resolution of a video by a factor set here. The value entered should be a positive integer. A value of 1 means that no downsampling will be performed. This is useful for rapidly troubleshooting the settings on videos with a very large field of view.

17) *Temporal Downsampling* is similar to Spatial Downsampling, except it downsamples the temporal resolution. This is useful for optimizing settings on very long, high frame rate (>15 Hz) videos.

18) *Temporal Iterations* is the number of iterations that will be performed to calculate the temporal components of ROIs. This should be set to at least 2 when not rapidly testing other parameters.

19) *Save Settings* allows you to save all settings under a specific name of your choosing. Settings are saved as .mat files.

20) *Load Settings* allows you to load any previously saved settings.

21) Once all settings are configured, click the *Run ROI Detection* button. Immediately after attempting to start ROI detection, an autosave file is automatically generated and updated as progress continues. This will automatically load the last used settings when the application is next used. Status of ROI detection will be displayed in the *Status* box.

22) After ROI detection is complete, the new file generated will be added to the bottom of the *Processed Files* list. A .mat file will be created with the complete set of data generated during The *Open* button will open the selected .mat file into a MATLAB workspace, if running source scripts.

23) *Clear List* clears the entire list of *Processed Files*.

ROI Refinement

1) From the initial GUI, click on the icon titled *ROI Refinement* to load the ROI Refinement GUI **(Figure 3)**. In the ROI Refinement GUI, click the *Load* button to choose any number of data files generated by *Automated ROI Detection* you would like to load. All files should be .mat format files. You can drag a box or use the select or shift key to select multiple files with the mouse. If you close the file select window and decide to add more files later, such as from a separate folder, they will add to the bottom of the list. If you accidentally try to add the same file multiple times, it will not be added to the list again and an error will display.

2) To remove a file that has been added to the *Files to Process* list, select the file with the mouse and click the *Remove* button.

3) To view an ROI, select an ROI by clicking on it, and then click the button *View ROI*. The left arrow button (<) will automatically select and load the previous ROI (lower in ROI number). The right arrow button (>) will automatically select and load the next ROI (higher in ROI number).

4) The ROI field is displayed in the top left corner. Isolated ROIs are displayed in the smaller figure on the right side of the screen. Below the ROI figures are the extracted traces. The upper trace is the fluorescence trace and the bottom trace is the deconvolved trace.

5) Set *Automated Exclusion* criteria. *Roundness* measures how similar an ROI is to a circle. This is useful when you are looking exclusively for neuron somata or other round ROIs. *Mean Width* indicates the mean width of an ROI and the relative size of the ROI. It is useful for removing ROIs that result from having too many components coalesce together into a single profile. *Activity Threshold* can be set to include ROIs that surpass a chosen activity threshold for a given number of consecutive frames. *Baseline Stability* is used to check if an ROI has a stable baseline throughout the imaging session by comparing the baseline at the beginning of recording with the baseline at the end.

6) *Borderline %* can be set to allow an ROI to have criteria slightly outside of the desired range. If an ROI has a number of criteria within the Borderline range equal to or less than the *Borderline Allowance*, the ROI will be included.

7) Click the *Run Refinement* button to automatically exclude ROIs based on your chosen criteria.

8) To manually exclude an ROI, select an ROI and click the *Exclude ROI* button. After being excluded, the ROI number in the list will be stricken out and the *Exclude ROI* button will become an *Include ROI* button.

9) Click the *Export* button to export your data in your selected format.

Supplemental Figure S1

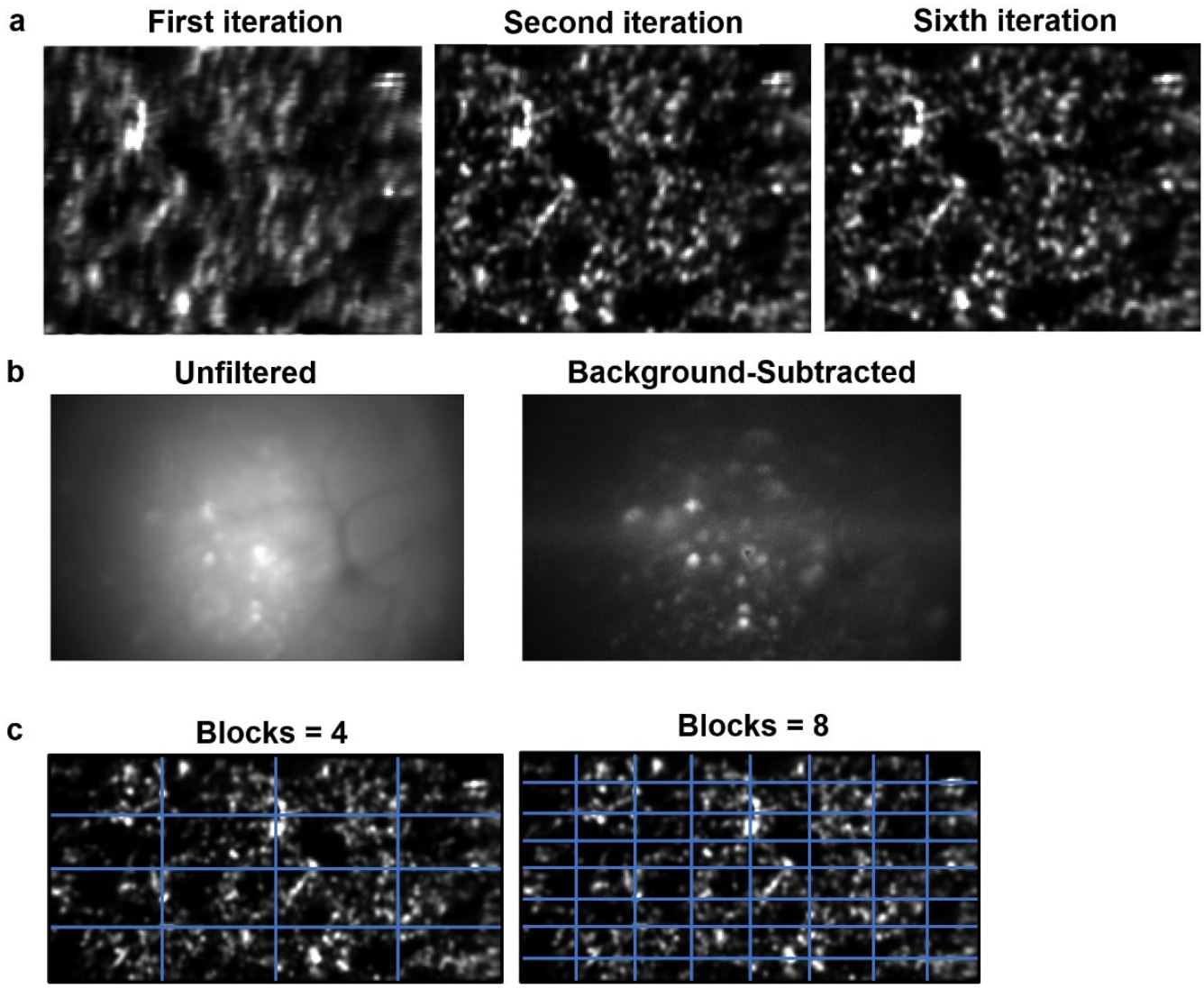

Figure S1: Effects of Motion Correction Options in EZcalcium

(a) Mean templates generated for the first, second, and sixth iteration of motion correction run on cortical axonal boutons. Accuracy of motion correction generally improves with number of iterations.

(b) Max-projection images of unfiltered and background subtracted videos obtained from CA1 Miniscope imaging.

(c) A representation of how the number of blocks in non-rigid motion correction segments an image prior to motion correction.

Supplemental Figure S2

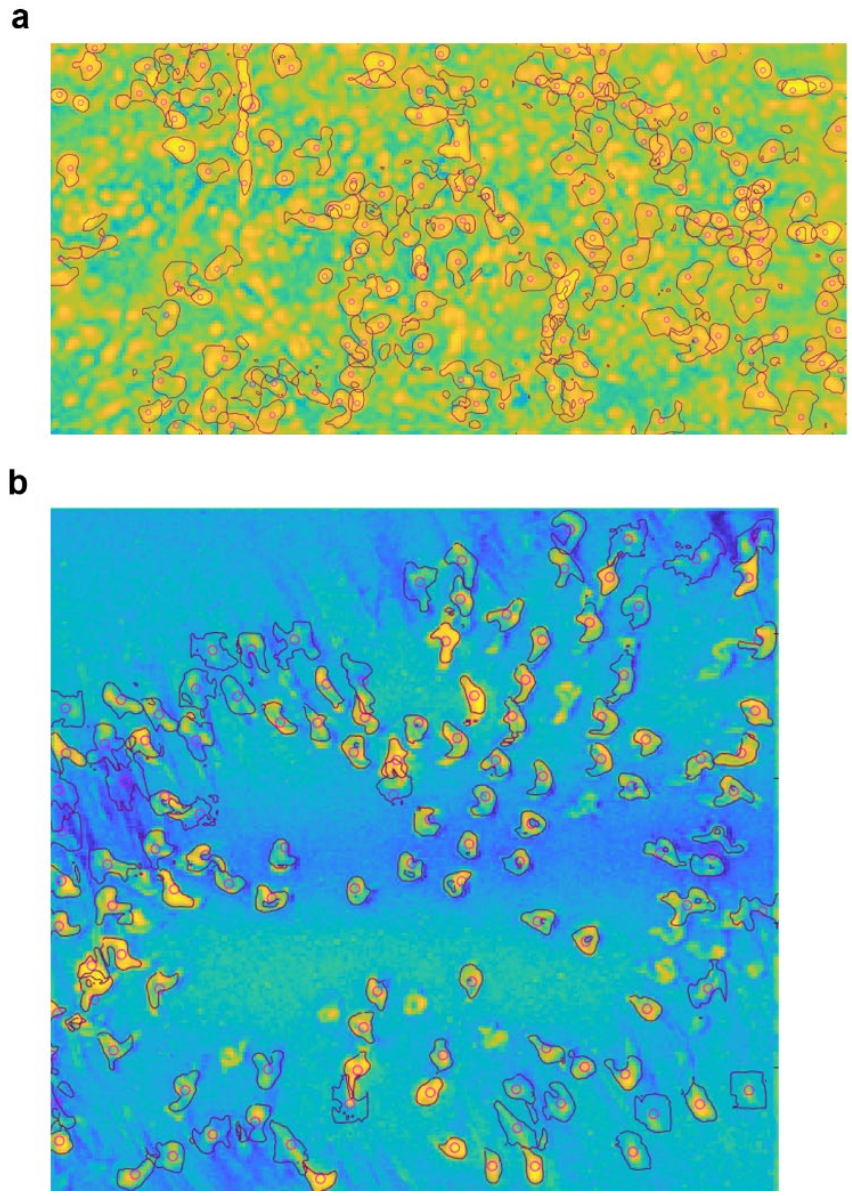

Figure S2: ROI segmentation in non-round ROIs

(a) ROI segmentation in mouse cortical axonal boutons. ROI centers are represented by magenta circles.

(b) ROI segmentation in *Drosophila melanogaster*

Chapter 2

Circuit-level defects underlying sensory abnormalities in a mouse model of autism

BACKGROUND

It has been suggested that phenotypic heterogeneity in autism might not reflect a unique cellular pathology, but rather a perturbation of network properties that emerge when neurons interact (Belmonte et al., 2004). In other words, the development of effective treatments for specific functional deficits in ASD will likely require understanding the circuit-level alterations involved. This is challenging in human patients, as the methods available to assess network-level correlates of sensory dysfunction (EEG or fMRI) lack single-neuron spatial resolution. Instead, it is necessary to record network activity *in vivo*, with cellular resolution, in mouse models of inherited ASDs (Goncalves et al., 2013, Lu et al., 2016). The EZcalcium toolbox I described in Chapter I is ideally suited for the analysis of calcium signals from neurons recorded in mouse models of autism. In this chapter I describe two experimental research projects that I significantly contributed to, in which we used in vivo 2-photon calcium imaging and EZcalcium to investigate the circuit alterations underlying atypical sensory processing in a mouse model of Fragile X syndrome, the leading inherited cause of autism.

Sensory dysfunction, especially hypersensitivity, occurs in many individuals with autism spectrum disorders (ASD) (Marco et al., 2011, Green et al., 2015). Sensory hypersensitivity (overreactivity) commonly affects auditory, tactile, or visual processing, and may present as defensiveness or avoidance (Marco et al., 2011, Green et al., 2015, Sinclair et al., 2017). Because it likely contributes to other ASD symptoms, such as anxiety, hyperarousal and sleep disturbances, attention deficit, stereotyped behaviors or rituals, and learning difficulties (Ben-Sasson et al., 2007, Sinclair et al., 2017), sensory overreactivity is a symptom of central significance in autism.

Fragile X Syndrome (FXS), the leading single-gene cause of cognitive impairment, is caused by a trinucleotide repeat expansion on the X chromosome that results in transcriptional silencing of the *Fmr1* gene coding for Fragile X mental retardation protein (FMRP) (Oberle et al., 1991, Pieretti et al., 1991). FMRP plays a key role in regulating many neuronal functions, particularly at synapses (Bagni and Zukin, 2019). Known targets of FMRP include transcription factors, growth factors, BK channels, and several GABA and glutamate receptors (Telias, 2019).

FXS is also the most common single-gene cause of autism (approximately 2% of ASD cases) (Wassink et al., 2001, Reddy, 2005), and the vast majority of FXS patients experience sensory abnormalities, such as tactile defensiveness (Butler et al., 1991, Hagerman et al., 1991). Additionally, the *Fmr1* knockout (KO) mouse model of FXS exhibits behavioral deficits analogous to human symptoms, including audiogenic seizures and increased startle responses (Bernardet and Crusio, 2006, Contractor et al., 2015). *Fmr1* KO mice also show increased intrinsic excitability, delayed GABA polarity switch, reduced inhibition, and network hypersynchrony (Contractor et al., 2015). However, how such hyperexcitability leads to behavioral sensory hypersensitivity or altered motion perception, or whether *Fmr1* KO mice even exhibit an avoidance response to tactile stimuli, has not been studied.

PART 1 – LOSS OF NEURONAL ADAPTATION TO REPETITIVE SENSORY STIMULATION IN FMR1 KO MICE

In order to examine the somatosensory system, we tested the hypothesis that specific abnormalities in sensory-evoked network activity in somatosensory cortex are associated with tactile defensiveness in *Fmr1* KO mice. In earlier studies not shown here (He et al., 2017), we demonstrated that 2-week-old and adult Fmr1 KO mice show maladaptive behavioral responses to repetitive whisker stimulation (20 bouts of whisker deflections at 10 Hz for 1 s each, with a 3 s inter-stimulus interval). Adult Fmr1 KO mice actively avoided the source of whisker stimulation, a behavior that closely mirrors tactile defensiveness in humans with FXS. Next, we performed *in vivo* two-photon calcium imaging of whisker-evoked activity in Layer (L) 2/3 neurons in barrel cortex in order to find the circuit-level correlates of sensory hypersensitivity in neocortex that give rise to the tactile defensiveness.

A reduced fraction of L2/3 neurons in barrel cortex respond to whisker stimulation in P14-16 *Fmr1* KO mice

Since maladaptive whisker-induced behavioral responses are already present in young *Fmr1* KO mice (He et al., 2017), we considered the underlying cortical circuit alterations in early postnatal development. P14-P16 is a critical period in sensory processing because the pattern of neuronal activity in barrel and visual cortices has just undergone a marked transition from high synchrony to a decorrelated and more computationally efficient state (Golshani et al., 2009, Rochefort et al., 2009, Frye and MacLean, 2016, O'Donnell et al., 2017). We tested three possible cortical mechanisms underlying sensory hypersensitivity in *Fmr1* KO mice: 1) Neurons exhibit higher-

than-normal firing rates in response to sensory stimulation; 2) A higher proportion of neurons respond to stimulation; and 3) Neurons show reduced adaptation (desensitization) to repetitive sensory stimuli. We considered the latter possibility especially likely, based on the lack of behavioral adaptation to whisker stimulation we observed in *Fmr1* KO mice.

To record whisker-evoked activity in L2/3 neurons of the barrel cortex, we used *in vivo* two-photon imaging of GCaMP6s signals (Chen et al., 2013) in P14-16 mice. First, we injected AAV1.Syn.GCaMP6s.WPRE.SV40 at P1, and then implanted a glass-covered cranial window at P10-12; we confirmed our targeting of barrel cortex with optical intrinsic signal imaging at P12-15 (see **Methods**, **Fig. 9a-c**). During imaging the animals were head-fixed, awake, and lightly sedated with isoflurane (<0.5%) and chlorprothixene. We first recorded spontaneous activity (205 s), followed by whisker-evoked activity (103 s), for which the animals received the same stimulation direction, timing and frequency as during the behavioral experiments (**Fig. 9d-e**). We did not find significant differences between WT and *Fmr1* KO mice in equivalent periods of spontaneous or whisker-evoked activity (Spontaneous: median fluorescence Z-score ± median absolute deviation was 4.73±0.43 for WT vs. 3.85±0.98 for *Fmr1* KO, p=0.31 by two-group comparison; Evoked: 3.13±0.39 for WT vs. 3.14±0.74 for *Fmr1* KO, p=1.00, **Fig. 9f**).

Next, we asked whether whisker stimulation recruits a larger-than-normal cohort of barrel cortex neurons in *Fmr1* KO mice. To do so, we calculated the proportion of L2/3 neurons that responded to whisker stimulation in a time-locked fashion (see **Methods, Fig. 9g**). Unexpectedly, we found that nearly half (45%) as many neurons exhibited an activity pattern that was time-locked to epochs

of whisker stimulation in *Fmr1* KO compared to WT mice (37.2±9.1% of WT neurons vs. 20.5±13.0% of *Fmr1* KO neurons; p=0.022 by two-group comparison, **Fig. 9h**). This suggests that the behavioral overreactivity that *Fmr1* KO mice manifest is not due to either exaggerated sensory-evoked firing of local networks in barrel cortex or to higher proportions of neurons within local networks being recruited by whisker stimulation.

Figure 9

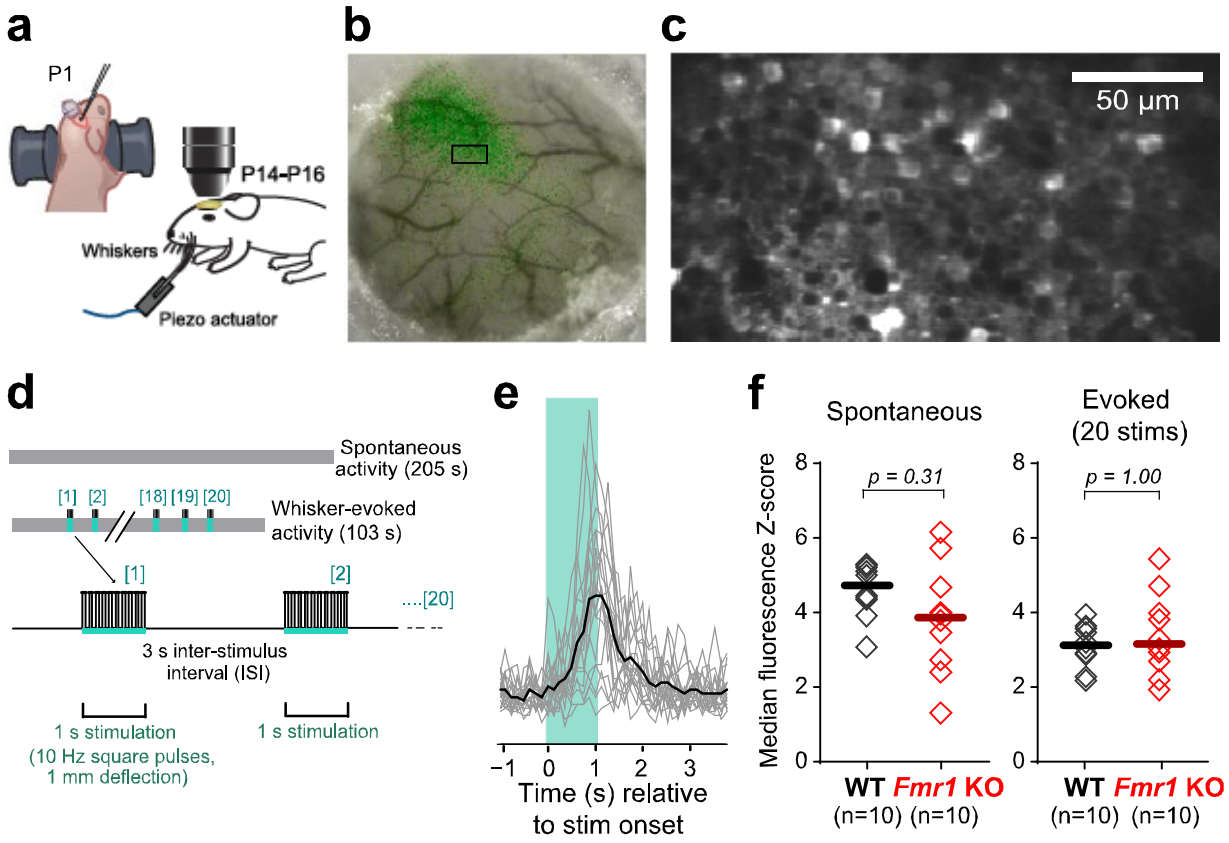
a
P1
P14-P16
Whiskers
Piezo actuator
b
c
50 µm
d
Spontaneous activity (205 s)
[1] [2] [18] [19] [20]
Whisker-evoked activity (103 s)
[1]
[2]
....[20]
3 s inter-stimulus interval (ISI)
1 s stimulation (10 Hz square pulses, 1 mm deflection)
1 s stimulation
e
−1 0 1 2 3
Time (s) relative to stim onset
f
Spontaneous
Evoked (20 stims)
Median fluorescence Z-score
p = 0.31
p = 1.00
WT Fmr1 KO
(n=10) (n=10)
WT Fmr1 KO
(n=10) (n=10)
g
Time-locked to whisker stim:
Cell 1
Cell 2
Non-time-locked:
Cell 3
Cell 4
0 10 20 30 40 50 60 70 80
Time (s)
h
Time-locked neurons (%)
p = 0.022
WT Fmr1 KO
(n=10) (n=10)

Figure 9: Differences in whisker-evoked network activity in *Fmr1* KO mice at P14-16

(a) Schematic of how AAV vector for GCaMP6s injection was injected into somatosensory cortex at P1 (*left*), and P14-16 *in vivo* imaging and whisker stimulation setup (*right*).

(b) Example cranial window over right somatosensory cortex at P14 and a map of whisker-evoked activity obtained with optical intrinsic signal imaging (green). Black box shows location of *in vivo* calcium imaging in (c).

(c) Example field of view of neurons in barrel cortex expressing GCaMP6s in the same mouse (at P15) shown in (b) at P15 (*xyt* SUM projection of 100 consecutive frames at 7.8 Hz).

(d) Protocol for recording spontaneous (1600 frames ≈ 205 s) and whisker-evoked activity (800 frames ≈ 103 s).

(e) Example of individual fluorescent signals extracted from one L2/3 neuron during 20 whisker stimulations (grey) and the mean signal (black), showing how single neurons in barrel cortex can respond to repeated stimulations.

(f) Median fluorescence Z-scores for spontaneous (left) and whisker-evoked activity (right) of L2/3 neurons in WT and *Fmr1* KO mice at P14-16 (n= 10 mice per genotype). Each diamond shows the median Z-score across all ROIs for one animal, for equivalent durations of spontaneous and evoked imaging (103 s). Bars represent group medians. In panels (f) and (h), P-values from two-group rank-based comparisons with 10,000 resamples, and Bonferroni correction in (f).

(g) Example fluorescence traces from two L2/3 neurons with activity that is time-locked (*top*) and from two different neurons with activity that is not time-locked (*bottom*) to whisker stimulation epochs (light grey bars).

(h) Local networks in barrel cortex of *Fmr1* KO animals have 50% fewer time-locked L2/3 neurons compared with WT.

Impaired adaptation of local whisker-evoked neuronal activity in P14-16 *Fmr1* KO mice persists into adulthood

Our experimental design allowed us to determine whether L2/3 neurons exhibit any adaptation during the 20 sequential whisker deflections, i.e., a reduction in firing with successive stimulations. We found that some L2/3 neurons showed robust adaptation, while others did not (**Fig. 10a-b**). When we analyzed whisker-evoked activity of all neurons imaged in each P14-16 WT animal, we found that the decrease in activity over time could be fit by an exponential curve with a decay constant τ= 4.1±1.3 stimulations (**Fig. 10c** left). However, the *Fmr1* KO mice did not show this clear decay in activity over time (**Fig. 10c** right). Based on the activity decay in the WT mice, we compared neuronal activity during the first five stimulations with activity during the last five stimulations. This analysis revealed that in WT mice at P14-P16, neuronal activity was significantly lower during the last five stimulations than during the first five (Z-scores: 3.56±0.27 vs. 2.02±0.38, p=0.028 by two-group comparison, **Fig. 10d**). In sharp contrast to WT mice, there was no significant change for *Fmr1* KO mice in neuronal activity from the first five to last five stimulations (2.95±1.01 vs. 2.59±0.99, p=1.000, **Fig. 10d**), suggesting that neural circuits in the mutant mice are unable to adapt to repetitive tactile stimuli.

We then wondered whether neuronal adaptation might only be evident in cells that responded to whisker stimulation in a time-locked fashion. The subpopulation of time-locked cells showed robust adaptation in both WT and *Fmr1* KO mice at P14-16 (WT p=0.011 by two-group comparison; *Fmr1* KO p=0.005, **Fig. 10e** left). Interestingly, while non-time-locked cells also

showed significant adaptation in WT mice, they did not in *Fmr1* KO mice (WT p=0.018; *Fmr1* KO p=1.000, **Fig. 10e** right). It appears that the lack of modulation of the activity of non-time-locked cells in the young *Fmr1* KO mice contributes to the defect in overall network adaptation during repetitive whisker stimulation. As a control for possible effects of continuous calcium imaging, we analyzed spontaneous activity of all ROIs during the equivalent "first five" and "last five" time bins and found no significant change within either genotype (**Fig. 10f**).

We also analyzed the correlation between the WT and *Fmr1* KO animals' proportions of time-locked neurons and the degree of their neuronal adaptation (Adaptation Index, see **Methods**) during the repeated stimulations. In WT mice, these two measures were significantly correlated (Spearman's ρ=0.733, p=0.021 by bootstrapping with 10,000 resamples) (**Fig. 10g**). In *Fmr1* KO mice, these two measures were not correlated (Spearman's ρ=0.273, p=0.436) (**Fig. 10g**). This finding indicates that the defect in L2/3 neuronal adaptation in the *Fmr1* KO mice is linked to their reduced proportion of time-locked neurons in local networks.

Figure 10

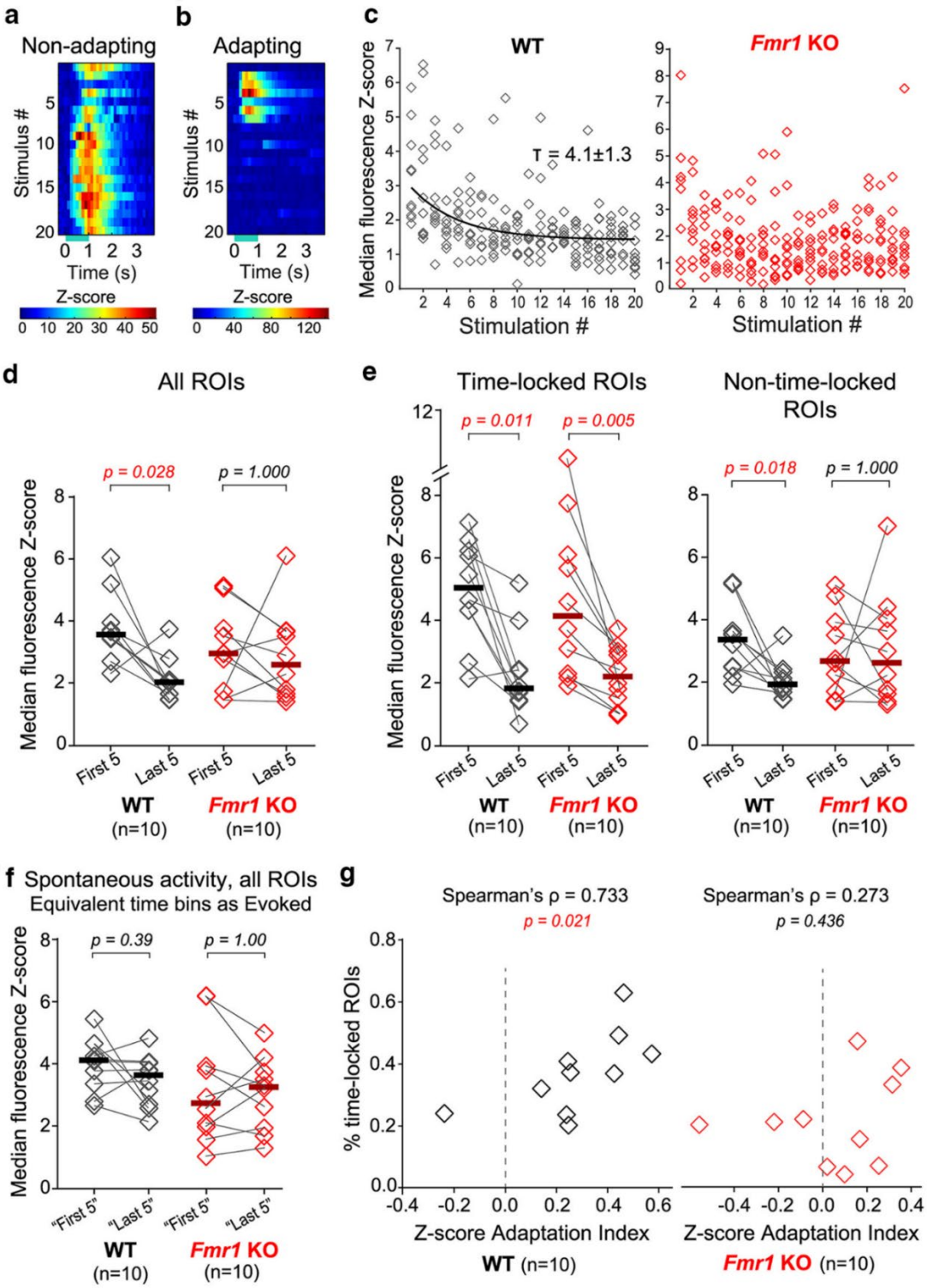
a
Non-adapting
Stimulus #
Time (s)
Z-score
b
Adapting
c
WT
Fmr1 KO
Median fluorescence Z-score
τ = 4.1±1.3
Stimulation #
d
All ROIs
p = 0.028
p = 1.000
First 5
Last 5
WT (n=10)
Fmr1 KO (n=10)
e
Time-locked ROIs
Non-time-locked ROIs
p = 0.011
p = 0.005
p = 0.018
p = 1.000
f Spontaneous activity, all ROIs
Equivalent time bins as Evoked
p = 0.39
p = 1.00
"First 5"
"Last 5"
g
Spearman's ρ = 0.733
p = 0.021
Spearman's ρ = 0.273
p = 0.436
% time-locked ROIs
Z-score Adaptation Index
WT (n=10)
Fmr1 KO (n=10)

Figure 10: Lack of adaptation of whisker-evoked activity in local networks of P14-16 *Fmr1* KO mice

(a-b) Heatmaps of activity from example P14-16 WT L2/3 neurons showing adaptation (a) or no adaptation (b) during 20 consecutive whisker stimulations (y-axis). For panels (a-c), median fluorescence Z-scores per animal were binned from 0.2 s before stimulation onset to 2.8 s after stimulation end.

(c) Median Z-scores for P14-16 WT mice (n=10) (left) and *Fmr1* KO mice (n=10) (right) during each stimulation bin, with exponential curve fit for neuronal activity in WT mice (see Methods). Each symbol represents a different animal (unknown sex).

(d) Median Z-scores of whisker evoked activity across all L2/3 neurons during the specified time bin during First 5 and Last 5 stimulations in WT and *Fmr1* KO mice at age P14-16 (n=10 mice per genotype). For panels (d-f), the median fluorescence Z-scores per animal were binned from the start of the first stimulation to 3 s after the end of the fifth stimulation. Each symbol represents a different animal. Bars represent group medians. P-values result from pairwise rank-based comparisons with 10,000 resamples and Bonferroni correction.

(e) Median Z-scores of whisker-evoked activity across time-locked and non-time-locked L2/3 neurons during First 5 and Last 5 stimulations in WT and *Fmr1* KO mice at P14-16.

(f) Median Z-scores of spontaneous activity across all ROIs at P14-16, binned using the same start and end times as used to analyze whisker-evoked activity in (d-e).

(g) Percentages of time-locked ROIs in WT and *Fmr1* KO mice at P14-16, plotted against Z-score Adaptation Indices, with Spearman's correlations. Adaptation Index = (Z-score during First 5 stimulations – Z-score during Last 5 stimulations) / (Z-score First 5 + Z-score Last 5). P-values from bootstrapping with 10,000 resamples.

We next tested whether a similar lack of neuronal sensory adaptation was evident in adult *Fmr1* KO mice, given that they show a clear avoidance response to repetitive whisker stimulation. We injected the AAV vector for GCaMP6s expression at 2-4 weeks before imaging and confirmed barrel cortex targeting using optical intrinsic signal imaging (see **Methods**). We did not find significant differences between adult WT and *Fmr1* KO mice (P34-74) in equivalent periods of spontaneous or whisker-evoked activity (p=1.00 by two-group comparison, **Fig. 11a**). In contrast to P14-16 mice, we did not find a difference in the proportion of time-locked L2/3 neurons between adult WT and *Fmr1* KO mice (p=0.35 by two-group comparison, **Fig. 11b**). However, whereas adult WT mice exhibited robust neuronal adaptation to repetitive whisker stimulation (Z-scores: 2.42±0.53 first five vs. 1.58±0.53 last five, p=0.012 by two-group comparison, **Fig. 11c**), adult *Fmr1* KO animals did not (2.18±0.34 first five vs. 2.20±0.50 last five, p=1.000, **Fig. 11c**).

In adult WT mice, both time-locked and non-time-locked cells showed adaptation (p=0.012 and p=0.066, **Fig. 11d**), but adult *Fmr1* KO mice did not show adaptation in either subset of cells (p=0.258 and p=1.000, **Fig. 11d**). There was again no change in spontaneous activity of all ROIs between the equivalent "first five" and "last five" time bins (**Fig. 11e**). On the whole, the data in adult mice was similar to the results in P14-P16 mice. The lack of modulation of the activity of non-time-locked cells in *Fmr1* KO mice (especially at P14-P16) appears to be responsible for the overall network adaptation defect observed during repetitive whisker stimulation.

Figure 11

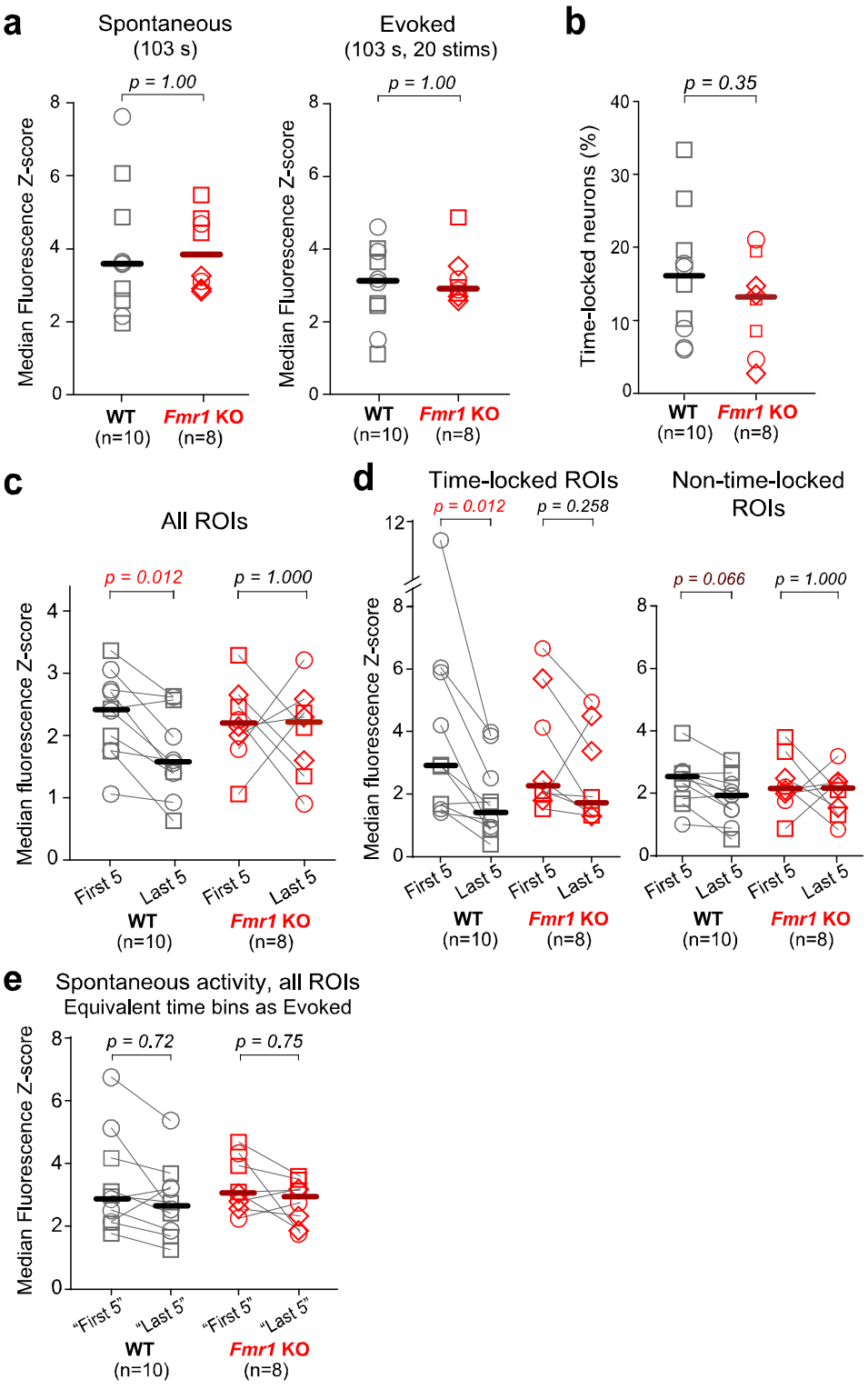
a
Spontaneous
(103 s)
Evoked
(103 s, 20 stims)
p = 1.00
p = 1.00
Median Fluorescence Z-score
WT
(n=10)
Fmr1 KO
(n=8)
b
p = 0.35
Time-locked neurons (%)
c
All ROIs
p = 0.012
p = 1.000
Median fluorescence Z-score
First 5
Last 5
d
Time-locked ROIs
Non-time-locked ROIs
p = 0.012
p = 0.258
p = 0.066
p = 1.000
e
Spontaneous activity, all ROIs
Equivalent time bins as Evoked
p = 0.72
p = 0.75
"First 5"
"Last 5"

Figure 11: Lack of adaptation of whisker-evoked activity in local networks of adult *Fmr1* KO mice

(a) Median Z-scores for spontaneous (left) and whisker-evoked activity (right) of L2/3 neurons in WT and *Fmr1* KO mice at P34-74 (n= 10 WT mice and n=8 *Fmr1* KO mice). Each circle shows the median Z-score across all ROIs for one animal, for equivalent durations of spontaneous and evoked imaging (103 s). In (a-e), circles represent female mice, squares represent male mice, and diamonds represent mice with unknown sex; bars represent group medians and p-values were obtained from two-group rank-based comparisons with 10,000 resamples, with pairwise comparisons and Bonferroni correction for (c-e).

(b) The proportion of time-locked neurons is not different between WT and *Fmr1* KO adult mice (n= 10 WT mice and n=8 *Fmr1* KO mice). Each symbol represents a different animal.

(c) Median Z-scores of whisker evoked activity across all L2/3 neurons during the specified time bin during First 5 and Last 5 stimulations in WT and *Fmr1* KO mice at age P34-74. For panels (c-e), the median Z-scores per animal were binned from the start of the first stimulation to 3 s after the end of the fifth stimulation.

(d) Median Z-scores of whisker-evoked activity across time-locked and non-time-locked L2/3 neurons during First 5 and Last 5 stimulations at P34-74.

(e) Median Z-scores of spontaneous activity across ROIs at P34-74, binned using the same start and end times as used to analyze whisker-evoked activity in (c-d).

PART 2 – IMPAIRED PERCEPTUAL LEARNING IN FRAGILE X SYNDROME IS MEDIATED BY PARVALBUMIN NEURON DYSFUNCTION AND IS REVERSIBLE

In this study, we investigated whether motion perception is impaired in Fmr1 KO mice. and then used calcium imaging to record from neurons in visual cortex to identify the underlying circuit-level alterations. First, we used an identical perceptual discrimination task in mice and humans and then deciphered specific circuit-level disruptions in *Fmr1* KO mice that bring about the altered behaviors. This parallel "mouse/human" perspective, derived from a circuit-level understanding of FXS symptoms, is a novel approach to targeting therapeutic interventions. Additionally, although many human psychophysical studies have demonstrated deficits in visual perception in individuals with FXS (Kogan et al., 2004, Farzin et al., 2008), whether fragile X mice also exhibit impaired visual processing is not known**.**

Impaired performance of *Fmr1 KO mice* in a 'reduced angle' visual discrimination task:

Fmr1 KO mice exhibit sensory hypersensitivity, which could impair their ability to learn and perform certain decision-making tasks. In studies not shown here, we found that *Fmr1* KO mice showed a significant delay in learning a Go/-No-Go visual discrimination task in which they must associate a 'preferred' visual stimulus (a drifting sinusoidal grating) with licking for a water reward, whereas they must withhold licking for a similar visual stimulus that is drifting in the orthogonal direction ('non-preferred') (Goel et al., 2018). However, Fmr1 KO mice eventually learned the task and performed at similar levels as control wild type mice.

Fmr1 KO mice are known to exhibit a broadening of receptive fields in somatosensory cortex (Arnett et al., 2014, Zhang et al., 2014, Juczewski et al., 2016). Similar broader tuning in V1, if it exists, could affect the discrimination of visual stimuli with very similar orientations. Therefore, we tested whether *Fmr1* KO mice would be particularly challenged by a reduced angle task, in which the difference in angle between the preferred and non-preferred orientation was gradually reduced to 7.5º, after the animals had learned the basic 90º task (**Fig. 12a-c**). Mice that had already maintained an expert-level performance (d' > 2) on the 90º task were tested for only two sessions at each of the reduced angle tasks (starting at 15 º, then 10 º and finally 7.5 º). The d' values shown **Fig. 12d** are an average of those two sessions. Overall there was a significant decrease in performance of the both groups when the angle between the orientations was reduced. (Friedman test: $F_{2,57} = 1.96$, $p = 5.5 \times 10^{-5}$). In particular there was a significant decrease in performance of *Fmr1 KO* mice on the 10º (Mann-Whitney test, p= .001) and 7.5 º (Mann-Whitney test, p= 0.02) task compared to WT. A difference in orientation angle of 15º did not impair the performance of either WT or *Fmr1 KO* mice (n= 10 for each); however, a further reduction down to 10º resulted in a significant reduction in *d'* values of *Fmr1 KO* mice, but not in WT controls (**Fig. 12d**; kruskal-wallis test; WT: $\chi^2_{2,28} = 12.66$, p= 0.03; Mann- Whitney test between 15º and 10º, p=0.09, and between 10º and 7.5º, p=0.03. kruskal-wallis test; *Fmr1 KO* : $\chi^2_{2,28} = 6.63$, p= 0.002; Mann-Whitney test between 15º and 10º, p=0.02, and between 10º and 7.5º, p=0.85.

A reduction in the angle difference to 7.5º did not further impair the performance of *Fmr1 KO* mice (p=0.85), indicating that many of the *Fmr1 KO* mice were already performing at chance on the 10º task. However, there was a further decline in the performance of WT mice (p=0.03) (**Fig. 12d**).

Figure 12

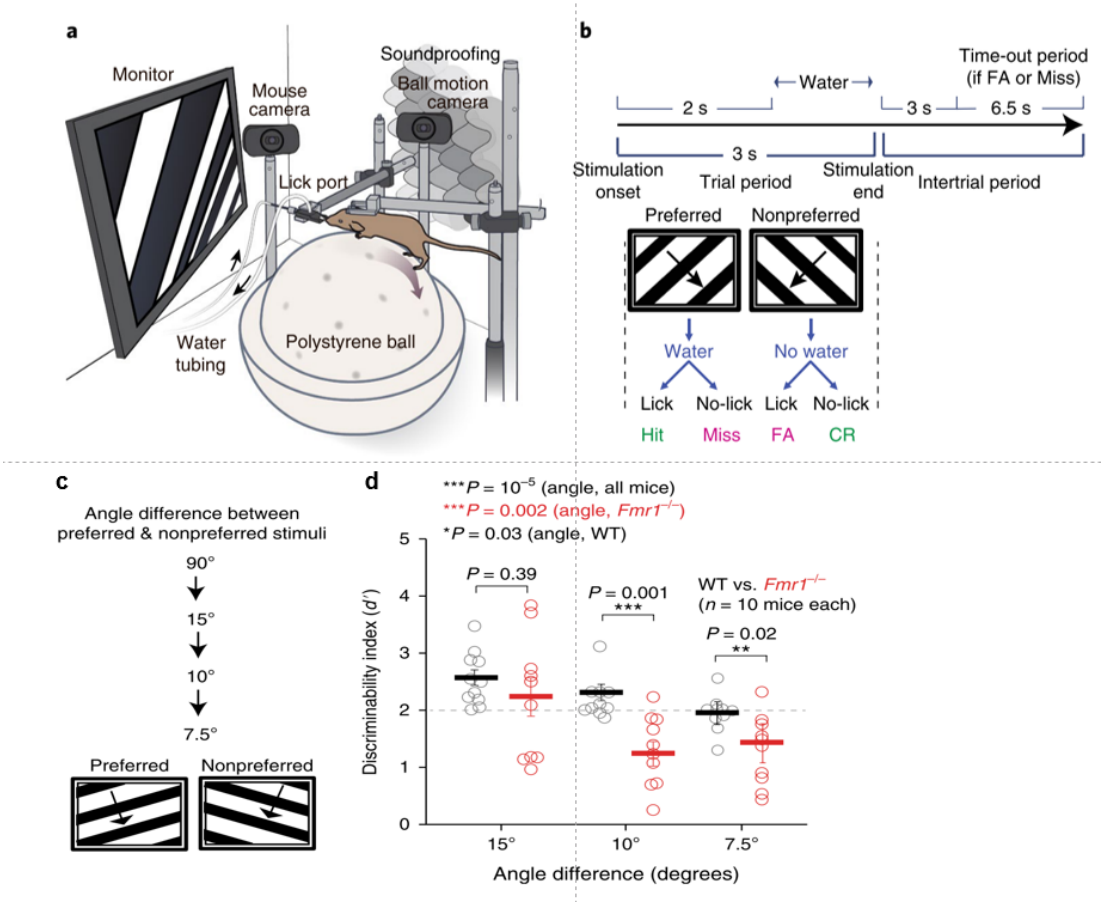

Figure 12: Reducing the angle between preferred and non-preferred stimuli impairs discrimination in *Fmr1* KO

a. Cartoon of the behavioral apparatus.

b. Timeline of an individual trial for the go/no-go visual discrimination task in water-deprived mice. FA, false alarm; CR, correct rejection.

c. After mice reached a d' > 2 on the 90º task (at 100% contrast), they were tested for only two sessions at the reduced angle tasks: 15 º, then 10 º and finally 7.5 º.

d. Selective impairment of *Fmr1 KO* mice in task performance when the angle difference between preferred and non-preferred stimuli drops below 15º.

Orientation tuning deficits in V1 correlate with task performance in *Fmr1 KO* mice

Having established a defect in perceptual learning in the fragile X mouse model that is relevant to the human disease, we next adopted a reverse engineering approach to identify the circuit- and neuronal-level alterations that might underlie the impaired visual discrimination. In light of various reports of cortical hyperexcitability and network hypersynchrony in *Fmr1 KO* mice (Goncalves et al., 2013, La Fata et al., 2014, Contractor et al., 2015) , we first investigated whether the perceptual learning deficit we observed in *Fmr1 KO* mice, was caused by abnormal orientation tuning of pyramidal cells in V1. To test this, we performed in vivo 2-photon calcium imaging in layer (L) 2/3 neurons in awake mice running on a floating polystyrene ball (**Fig. 13a-c**; Materials and methods). A rAAV to express GCaMP6s (Chen et al., 2013) was injected in V1 following stereotaxic coordinates, and successful targeting was confirmed using intrinsic signal imaging (**Fig. 13b**). We recorded both spontaneous and visually evoked activity from L2/3 neurons in mice that were fully acclimated to the experimental rig and running vigorously throughout the calcium imaging session (**Fig. 13c**). For the latter, WT and *Fmr1 KO* mice (n= 9 and 10, respectively) were presented with four sequential presentations of sinusoidal gratings drifting in 8 different directions (4 orientations), at random (**Fig. 13d**; Materials and methods). Although previous studies have reported hyperexcitable cortical circuits in *Fmr1 KO* mice (reviewed in (Contractor et al., 2015)), we did not observe a significant increase in either spontaneous or visually evoked activity in *Fmr1 KO* mice (**Fig. 13e**).

Despite the seemingly normal frequency of visually evoked activity in *Fmr1 KO* mice, mutant mice had a significantly lower percentage of orientation selective (OS) cells in L2/3 (**Fig. 13f**; 49.5

± 2.1% in WT vs. 31.2 ± 4.6% in *Fmr1 KO*; p= 0.003, t-test). Importantly, when we trained these mice on the visual discrimination task, we found a significant inverse correlation between the percentage of OS cells and the number of days it took animals to reach a d' > 2 (**Fig. 13g**; r= -0.605, p= 0.006). This implies that, with fewer available OS cells in V1, *Fmr1 KO* mice had more difficulty discriminating between two different orientations, particularly when the difference was small (**Fig. 12 a-d**). In addition, in vivo calcium imaging revealed that L2/3 neurons in V1 of *Fmr1 KO* mice had a significantly broader tuning compared to those in WT mice (**Fig. 13h;** 36.7 ± 1.0^{o} in WT vs. 43.3 ± 1.4^{o} in *Fmr1 KO*; p= 0.002, t-test). This 6.6^{o} difference in the mean tuning width of pyramidal neurons in V1 between WT and *Fmr1 KO* mice, though slight, might be sufficient to explain why *Fmr1 KO* mice can discriminate at 15^{o} but not at 10^{o}. Additionally, we found a significant correlation between the tuning width of L2/3 cells and the number of days it took the animals to reach a d' > 2 (r= 0.48, p= 0.041).

Figure 13

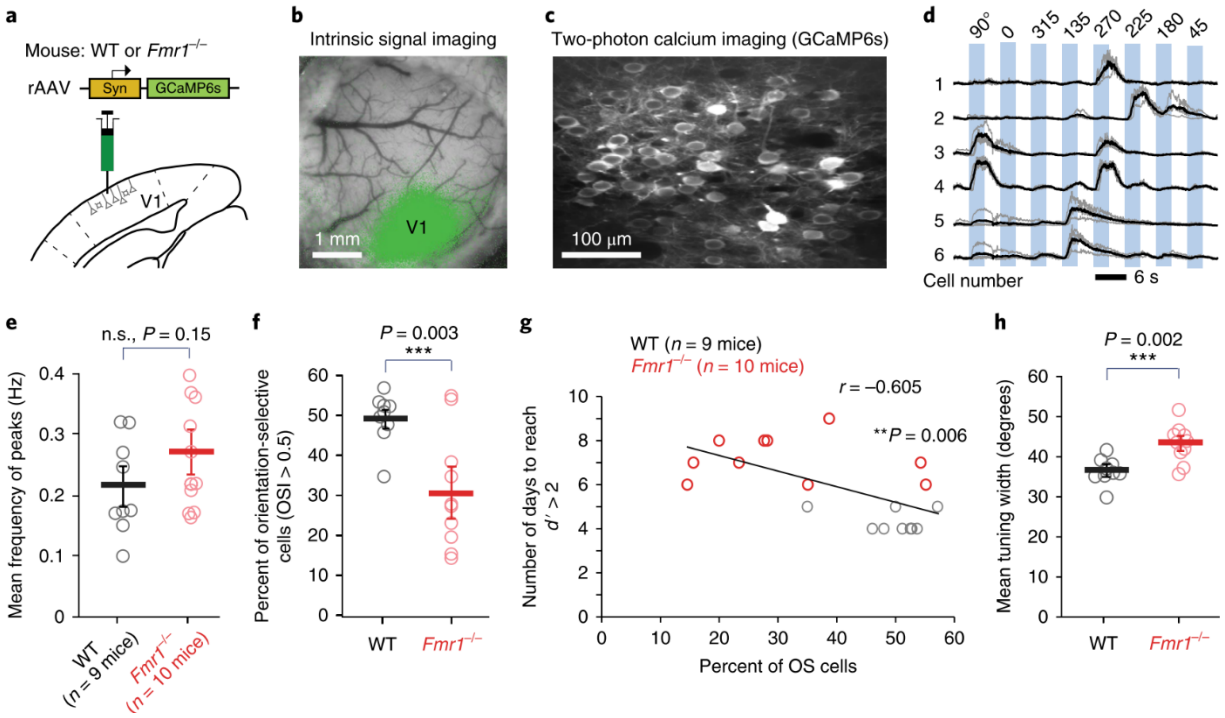
a
Mouse: WT or Fmr1−/−
rAAV
Syn
GCaMP6s
V1
b
Intrinsic signal imaging
1 mm
V1
c
Two-photon calcium imaging (GCaMP6s)
100 µm
d
90° 0 315 135 270 225 180 45
1 2 3 4 5 6
Cell number
6 s
e
n.s., P = 0.15
Mean frequency of peaks (Hz)
WT (n = 9 mice)
Fmr1−/− (n = 10 mice)
f
P = 0.003
***
Percent of orientation-selective cells (OSI > 0.5)
WT
Fmr1−/−
g
WT (n = 9 mice)
Fmr1−/− (n = 10 mice)
r = –0.605
**P = 0.006
Number of days to reach d' > 2
Percent of OS cells
h
P = 0.002
***
Mean tuning width (degrees)
WT
Fmr1−/−

Figure 13: Orientation tuning deficits in V1 correlate with task performance in *Fmr1 KO* mice.

a. Cartoon of rAAV-GCaMP6s injection into V1.

b. Intrinsic signal imaging was then performed 2-3 weeks after rAAV injection to confirm appropriate targeting of V1 (green map).

c. Representative field of view for in vivo two-photon calcium imaging experiment in V1. Imaging was performed 3-4 weeks after rAAV injection at 15 fps.

d. Example traces of changes in GCaMP6s fluorescence intensity (ΔF/F) for 6 representative neurons in V1 that exhibit a range of responses from narrow tuning (cell 1) to broad tuning (cells 2 & 3). Responses to single trials are shown in gray, averages of 4 responses are in black.

e. Visual evoked activity (as measured by the frequency of fluorescence peaks) is similar between WT and *Fmr1 KO* mice. Symbols in panels E-H represent different mice. Unpaired, one-tailed Student t-test was used for panels E-F, H.

f. The percentage of orientation selective neurons in V1 is significantly lower in *Fmr1 KO* mice.

g. Inverse correlation between the percentage of orientation selective neurons in V1 and performance on the visual discrimination task (as measured by the number of days required to reach a d'>2).

h. The mean orientation tuning width for V1 neurons is significantly higher in *Fmr1 KO* mice. Tuning width also correlates with task performance

Reduced activity of parvalbumin cells in V1 in *Fmr1 KO* mice

Abnormal V1 network dynamics pertaining to orientation selectivity and tuning width could be the result of dysfunction in parvalbumin (PV) interneurons, the most prevalent inhibitory neuron in V1 (Gonchar and Burkhalter, 1997). PV cells exhibit very broad orientation tuning by simply responding to all orientations, since they receive local input from a wide range of orientation tuned pyramidal cells (Hofer et al., 2011, Zariwala et al., 2012, Runyan and Sur, 2013). Furthermore, selective stimulation of PV cells in V1 with channelrhodopsin-2 leads to improved feature selectivity and visual discrimination(Lee et al., 2012). For these reasons, we tested the hypothesis that PV cells were hypoactive in fragile X mice. We used in vivo calcium imaging to record the activity of PV neurons in V1 of WT and *Fmr1 KO* mice (n= 6 and 7, respectively) that expressed Td-Tomato in PV neurons (PV-Cre mice x ai9 mice; see Materials and methods). At the time of the cranial window surgery, we injected a Cre-dependent virus into V1, to selectively express GCaMP6s in PV cells (**Fig. 14a, b**). Our calcium imaging recordings revealed stark differences in the activity of PV cells between WT and *Fmr1 KO* mice; whereas traces of PV cell activity in WT mice showed the expected broadly tuned, non-selective responses to visual stimuli, traces of PV cells in *Fmr1 KO* mice exhibited reduced visually evoked activity (**Fig. 14c**). (**Fig. 14d**), *Fmr1 KO* mice exhibited a significantly lower frequency of events triggered by visual stimuli (**Fig. 14d;** 4.1 ± 0.5 for WT vs. 2.1 ± 0.5 for *Fmr1 KO*; p= 0.03, Mann-Whitney test; **14e**; 1.8 ± 0.5 for WT vs. 0.3 ± 0.1 for *Fmr1 KO*; p= 0.03, Mann-Whitney test). One of our criteria for selecting PV cells for analysis in both WT and *Fmr1 KO* mice was that they exhibit at least one calcium transient in the recordings (Materials and methods), and neither the proportion of active PV cells (**Fig. 14f**; p= 0.7, Mann-Whitney test), nor the amplitude or frequency of spontaneous calcium transients in PV

cells, were significantly different between WT and *Fmr1 KO* mice. We also found a significantly lower fraction of stimulus-responsive PV cells in *Fmr1 KO* mice (**Fig. 14g**; 0.7 ± 0.02 for WT vs. 0.4 ± 0.03 for *Fmr1 KO*; $p < 10^{-5}$, t-test), which would also ultimately be expected to affect the functional output of V1.

Figure 14

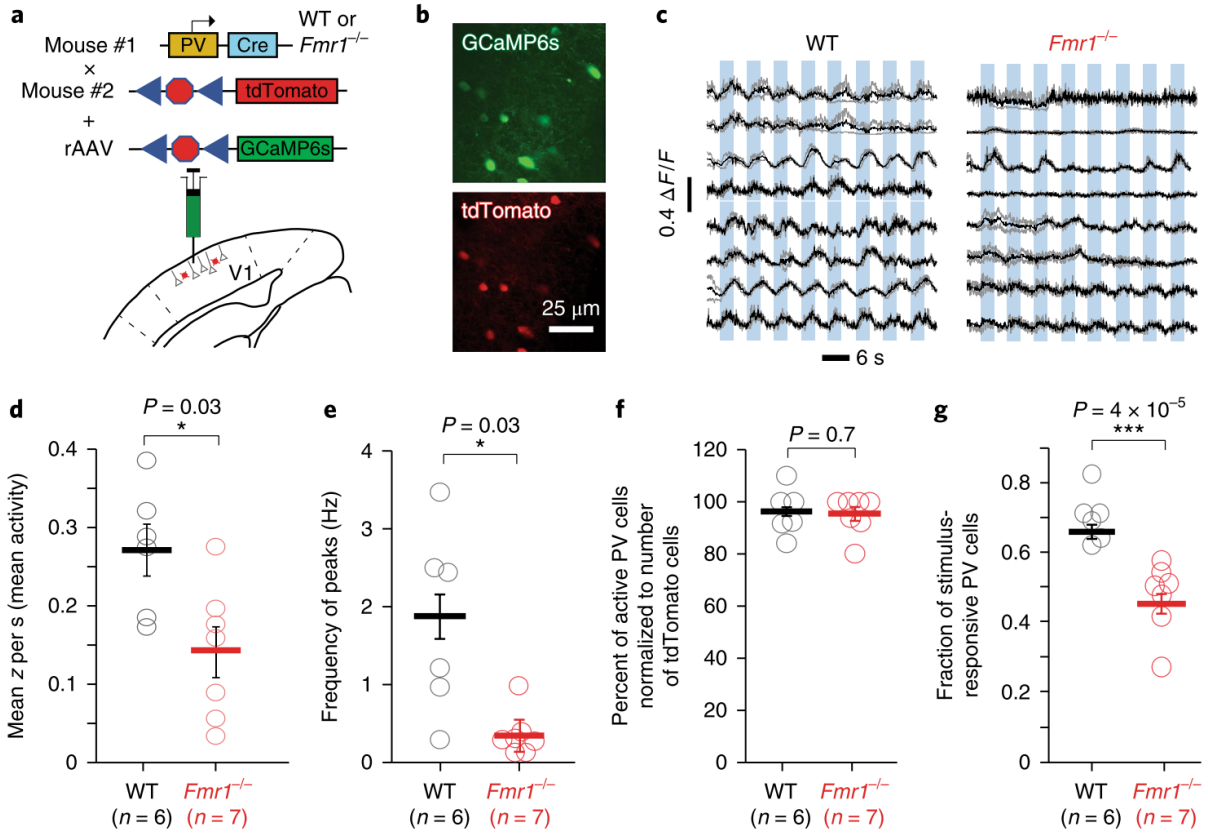
a
Mouse #1
PV
Cre
WT or Fmr1−/−
×
Mouse #2
tdTomato
+
rAAV
GCaMP6s
V1
b
GCaMP6s
tdTomato
25 µm
c
WT
Fmr1−/−
0.4 ΔF/F
6 s
d
P = 0.03
*
Mean z per s (mean activity)
WT (n = 6)
Fmr1−/− (n = 7)
e
P = 0.03
*
Frequency of peaks (Hz)
WT (n = 6)
Fmr1−/− (n = 7)
f
P = 0.7
Percent of active PV cells normalized to number of tdTomato cells
WT (n = 6)
Fmr1−/− (n = 7)
g
P = 4 × 10−5
***
Fraction of stimulus-responsive PV cells
WT (n = 6)
Fmr1−/− (n = 7)

Figure 14: Parvalbumin interneurons in V1 in *Fmr1 KO* mice show reduced functional output.

a. Cartoon of strategy for selective GCaMP6s expression in PV interneurons.

b. Representative field of view for in vivo 2-photon calcium imaging in PV neurons expressing GCaMP6s (green) and Td-Tom (red).

c. Example traces of changes in GCaMP6s fluorescence intensity (ΔF/F) for 8 representative PV neurons in V1 from 4 WT (left) and 4 *Fmr1 KO* mice (right). Responses to 8 different directions from single trials are shown in gray, while the averages of 4 trials are in black.

d. The magnitude of visual evoked calcium transients (as measured by the mean fluorescence Z-scores) is similar between WT and *Fmr1 KO* mice (sample size in parenthesis). Symbols in panels d-j represent different mice. Unpaired, one-tailed Student t-test was used for panels d-g.

e. The frequency of visually evoked calcium transients in PV neurons is significantly lower in *Fmr1 KO* mice.

f. WT and *Fmr1 KO* mice and similar percentages of PV cells that were active.

g. The fraction of visually-responsive PV cells is significantly reduced in *Fmr1 KO* mice. There is an inverse correlation between the fraction of stimulus responsive PV cells and behavioral performance.

A DREADD strategy that restores PV cell activity and orientation tuning in V1 accelerates learning of the visual task in *Fmr1 KO* mice.

Based on the finding that PV cells were indeed hypoactive in *Fmr1 KO* mice, we hypothesized that a successful manipulation of PV cell activity that would restore their output in these animals, might also improve their performance on the visual discrimination task. Hence, we used a Designer Receptors Exclusively Activated by Designer Drugs (DREADD) approach (Armbruster et al., 2007) (see Materials and methods) to selectively express the excitatory hM3Dq receptor in PV cells of *Fmr1 KO* mice (n= 6; **Fig. 15a**). We then used the hM3Dq ligand, clozapine-N-oxide (CNO, 5 mg/kg, i.p.), to excite PV cells and increase their output in these *Fmr1 KO*$^{, hM3Dq}$ mice. Overexpressing hM3Dq in PV cells alone (before administering CNO) did not affect visually evoked activity of PV cells in *Fmr1 KO*$^{, hM3Dq}$ mice. In contrast, 30 min after a single CNO injection, we observed a robust increase in visually evoked PV cell output in these *Fmr1 KO*$^{, hM3Dq}$ mice (**Fig. 15 b-e**); Spontaneous activity was unaffected by CNO. Specifically, we observed a significant increase in both the frequency of visually evoked calcium transients in PV cells of *Fmr1 KO*$^{, hM3Dq}$ mice (**Fig. 15c**; 0.2 ± 0.02 before CNO vs. 0.32 ± 0.05 after CNO; p= 0.02, t-test), and in the frequency of those events (**Fig. 15d**; 0.3 ± 0.04 before CNO vs. 0.6 ± 0.1 after CNO; p= 0.03, t-test). The fraction of stimulus responsive PV cells in *Fmr1 KO*$^{, hM3Dq}$ mice was also significantly increased by CNO, restoring it to WT levels (**Fig. 15e**; 0.4 ± 0.06 before CNO vs. 0.7 ± 0.04 after CNO; p= 0.001, t-test). Importantly, the fact that we could increase the activity of PV cells with DREADDs supports the notion that PV cells were not silent in *Fmr1 KO* mice due to poor health. Also, the proportion of PV cells that was active did not change after CNO

administration (not shown), suggesting that the DREADD effect on the fraction of visually responsive PV neurons was not due to simply making previously silent cells more active. Note that the data from *Fmr1 KO* mice (before CNO group) in Fig. 15 c, d and e is similar to the data from *Fmr1 KO* mice in Fig. 14 d, e and g indicative of robust replication of our findings.

Having restored visually evoked PV cell activity in *Fmr1 KO*$^{/,\ hM3Dq}$ mice to near normal WT levels, we hypothesized that we might be able to reverse the delay in learning the visual discrimination task. A subset of the DREADD-expressing *Fmr1 KO* mice were therefore trained on the standard visual discrimination task (90º angle) and injected with CNO, ~30 min prior to each training session. This chemogenetic manipulation resulted in a leftward shift in the learning curve (i.e., faster learning) of CNO-treated *Fmr1 KO*$^{,\ hM3Dq}$ mice (**Fig. 15f**), indicating that we were able to rescue the learning impairment by acutely elevating the PV cell output. CNO led to a significant reduction in the number of days required to reach expert level (d' > 2) on the visual discrimination task compared to *Fmr1 KO* mice (**Fig. 15g**; WT: 3.5 ± 0.2 d, *Fmr1 KO*: 6.0 ± 0.4 d; *Fmr1 KO*$^{,\ hM3Dq}$ with CNO: 3.7 ± 0.3 d; *Fmr1 KO* with CNO: 6.4 ± 0.8 d; $\chi^2_{3,55,}$ p= 5.2 X 10^{-5}, Kruskal-Wallis test; Mann-Whitney test between *Fmr1 KO* and *Fmr1 KO*$^{,\ hM3Dq}$ with CNO p=0.004;). Importantly injection of CNO alone in the absence of DREADDs in *Fmr1 KO*, did not rescue behavior (**Fig 15g**, Mann–Whitney test, p= 0.8) To come full circle back to OS cells in V1, we also tested whether the DREADD manipulation on PV cells would be sufficient to affect the properties of pyramidal neurons in the circuit. Calcium imaging with rAAV-GCaMP6s in a group of *Fmr1 KO*$^{,\ hM3Dq}$ mice revealed that CNO administration significantly raised the proportion of orientation selective pyramidal cells and showed a trend towards sharper tuning (**Fig. 15h, i**; p=

0.02 and 0.07, respectively; t-test). Notably, the relationship between PV cell output and behavior was apparent from the negative correlation between the fraction of stimulus responsive PV cells and the number of days needed to reach a d' > 2 (**Fig. 15j**; r -0.753, p= 0.0007). This relationship showed clearly how *Fmr1 KO*$^{, hM3Dq}$ mice treated with CNO were not distinguishable from WT mice. Additionally, the delayed learning observed in *Fmr1 KO* mice that did not receive CNO replicates our finding in Fig. 1 and 2 and this further corroborates our primary result of impaired visual discrimination in *Fmr1 KO* mice.

Figure 15

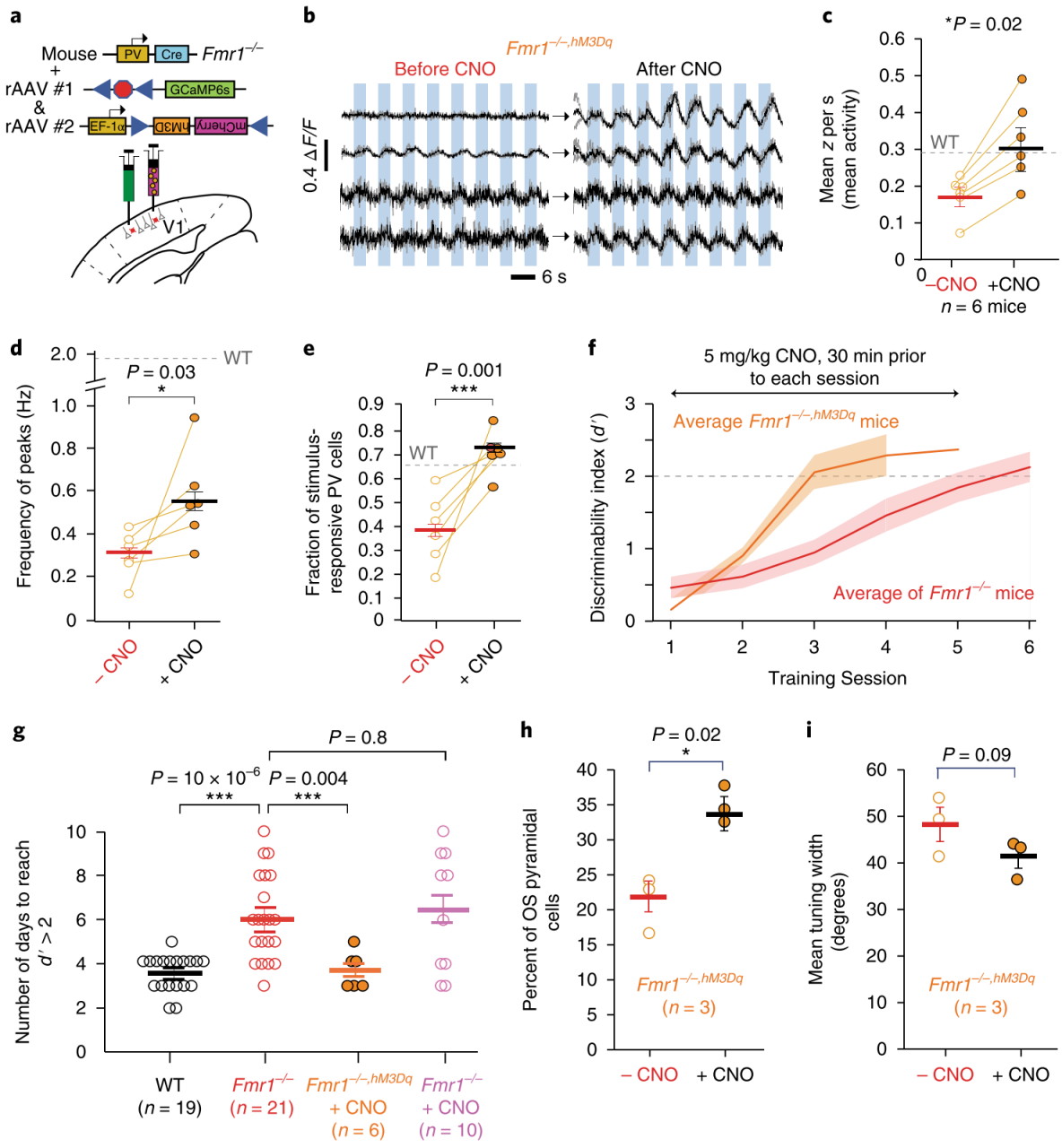
a
Mouse
PV
Cre
Fmr1−/−
+
rAAV #1
GCaMP6s
&
rAAV #2
EF-1α
hM3D
mCherry
V1
b
Fmr1−/−,hM3Dq
Before CNO
After CNO
0.4 ΔF/F
6 s
c
*P = 0.02
Mean z per s (mean activity)
WT
–CNO
+CNO
n = 6 mice
d
P = 0.03
WT
Frequency of peaks (Hz)
– CNO
+ CNO
e
P = 0.001
Fraction of stimulus-responsive PV cells
WT
– CNO
+ CNO
f
5 mg/kg CNO, 30 min prior to each session
Average Fmr1−/−,hM3Dq mice
Average of Fmr1−/− mice
Discriminability index (d′)
Training Session
g
P = 0.8
P = 10 × 10−6
P = 0.004
Number of days to reach d′ > 2
WT (n = 19)
Fmr1−/− (n = 21)
Fmr1−/−,hM3Dq + CNO (n = 6)
Fmr1−/− + CNO (n = 10)
h
P = 0.02
Percent of OS pyramidal cells
Fmr1−/−,hM3Dq (n = 3)
– CNO
+ CNO
i
P = 0.09
Mean tuning width (degrees)
Fmr1−/−,hM3Dq (n = 3)
– CNO
+ CNO

Figure 15: A DREADD strategy that restores normal PV cell activity in V1 rescues delayed learning in *Fmr1 KO* mice.

a. Cartoon of strategy for selective rAAV-EF1a-DIO-hM3D(Gq)-mCherry expression in PV interneurons of *Fmr1 KO* mice.

b. Example of GCaMP6s traces for 4 representative PV neurons in V1 from 4 different *Fmr1 KO*, hM3Dq mice before and after ~30min after i.p. injection of clozapine N-oxide (CNO).

c, d. The activity of PV cells, as measured by both median fluorescence Z-score (c) or the frequency of calcium transients (d), in *Fmr1 KO, HM3Dq* mice increases significantly after CNO administration. Symbols in panels J-L represent different mice. A one-tailed, unpaired Student t-test was used for panels I-K.

e. The fraction of stimulus-responsive PV cells also increases significantly after CNO. Note that the fraction of visually responsive PV cells was comparable between *Fmr1 KO* mice expressing DREADDs (before CNO) and *Fmr1 KO* mice in **Fig. 4g**.

f. *Fmr1 KO, HM3Dq* mice (n= 6; treated with CNO 30 min prior to each session) learned the basic 90º task in ~3 d on average. The rate of learning for *Fmr1 KO* mice (from **Fig. 1e**) is shown for comparison. The solid line indicates the mean, and the shaded area shows the standard error. The dashed line at d'= 2 indicates expert performance threshold.

g. Fmr1 KO, HM3Dq mice treated with CNO learned the basic 90º task significantly faster than *Fmr1 KO* mice and as fast as WT mice. Repeated measures ANOVA.

h. The percentage of OS pyramidal neurons in *Fmr1 KO*$^{, HM3Dq}$ mice was significantly higher after CNO administration. Student t-test.

i. There was a non-significant trend toward reduced tuning width of pyramidal neurons in *Fmr1 KO*$^{, HM3Dq}$ mice after CNO administration.

j. There is a strong inverse correlation between task performance (days to reach d'>2) and the fraction of stimulus-responsive PV cells in V1.

Fragile X patients exhibit similar defects in visual discrimination as *Fmr1 KO* mice

It was recently argued that the absence of directly comparable behavior paradigms between human and animal studies is a real impediment to progress in translational research for autism (Robertson and Baron-Cohen, 2017). It might even explain, in part, the failure of clinical trials in FXS (Mullard, 2015). In order to assess the translational potential of our findings of impaired visual discrimination (and, by extension, the associated circuit dysfunction) in a mouse model of FXS, we next asked whether the same perceptual learning task could be applied to humans with FXS. We implemented the same paradigm as in mice with relatively minor modifications, to make it suitable for individuals with FXS (**Fig. 16a, b**; Materials and methods). Healthy control human participants and FXS participants (n= 8 each) were administered the task. Healthy controls learned the basic 90^{o} task with high discriminability very quickly (within the first ten trials) in a single training session (**Fig. 16c**). Performance declined slightly in some healthy control participants at reduced angles, but on average, this was not significant. FXS participants showed a trend towards a lower d' at the 15^{o} task compared with 90^{o} or 45^{o} tasks however this did not reach significance ($p= 0.06$; kruskal-wallis test). However there was a robust decrease in d' at all the angles measured. (90^{o}, $p=0.001$; 45^{o}, $p=0.01$; 15^{o}, $p=0.001$; Mann –Whitney test). Thus, FXS participants and *Fmr1 KO* mice exhibit strikingly similar visual perception deficits for ambiguous stimuli with similar orientations. This suggests that a discrimination task like the one we used could eventually be used as biologically-based measure of sensory processing in human clinical trials.

Figure 16

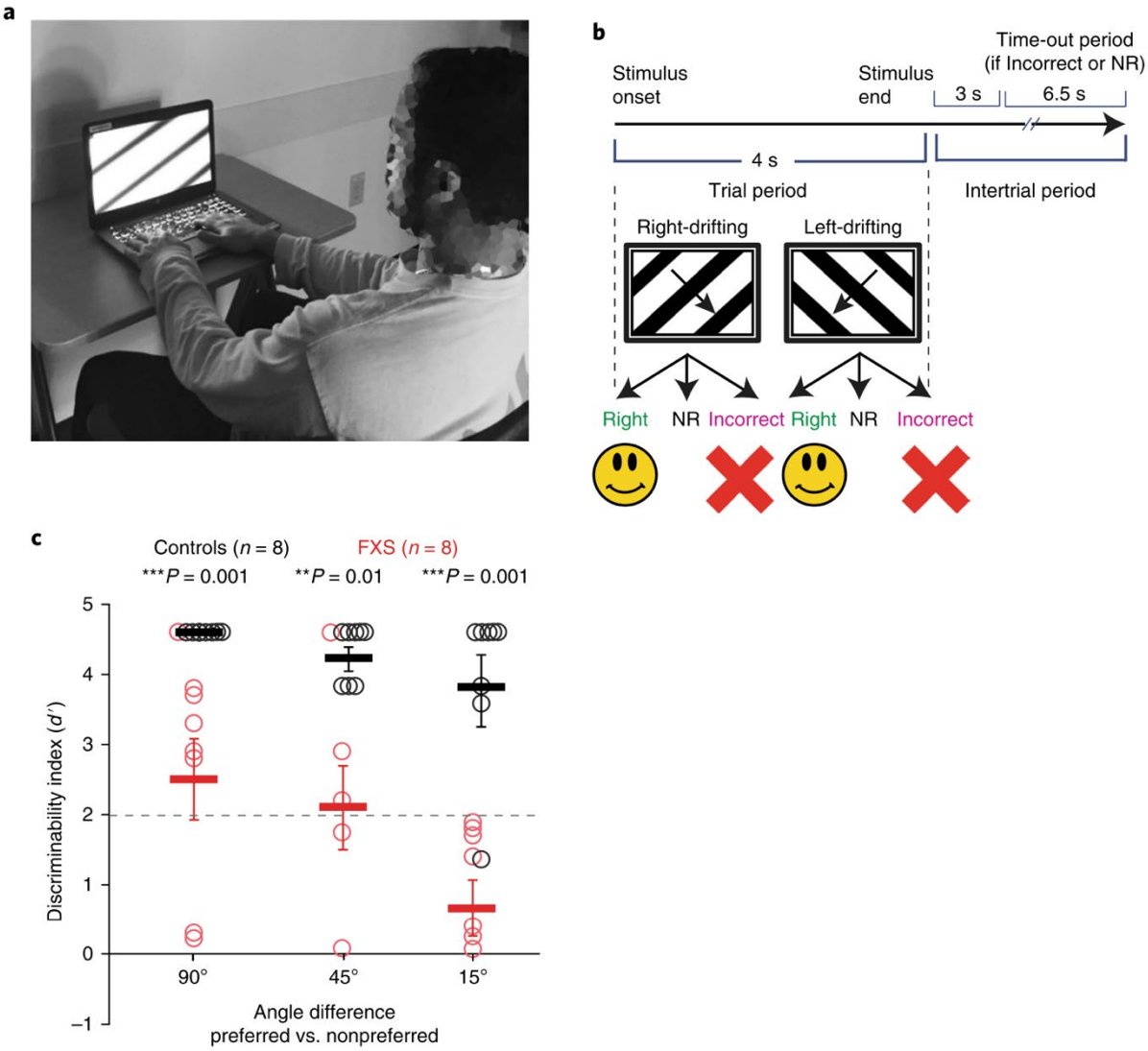
a
b
Time-out period
(if Incorrect or NR)
Stimulus
onset
Stimulus
end
3 s
6.5 s
4 s
Trial period
Intertrial period
Right-drifting
Left-drifting
Right
NR
Incorrect
Right
NR
Incorrect
c
Controls (n = 8)
FXS (n = 8)
***P = 0.001
**P = 0.01
***P = 0.001
Discriminability index (d')
5
4
3
2
1
0
−1
90°
45°
15°
Angle difference
preferred vs. nonpreferred

Figure 16: Fragile X patients exhibit similar defects in visual discrimination as *Fmr1 KO* mice

a. Photograph of a FXS subject performing the visual discrimination task.

b. Timeline of an individual trial for the visual discrimination task in human subjects. NR: no response.

c. Task performance at different angles between orientation #1 and orientation #2 for FXS subjects and age-matched control participants. Individuals with FXS are able to perform the 90^{o} visual discrimination task with d'> 2 but they exhibit a significantly lower d' than controls with the reduced angle task.

MATERIALS AND METHODS

Materials: Unless otherwise noted, materials were purchased from Sigma-Aldrich.

Experimental animals

All experiments followed the U.S. National Institutes of Health guidelines for animal research, under an animal use protocol (ARC #2007-035) approved by the Chancellor's Animal Research Committee and Office for Animal Research Oversight at the University of California, Los Angeles. Most experiments used male and female FVB.129P2 WT mice (JAX line 004828) and *Fmr1* KO mice (JAX line 004624) (Bakker et al., 1994), with the exception of the experiments in **Fig. 3**, which used male and female PV-Cre mice (JAX line 008069) that were crossed to the Ai9 (Td-Tom) reporter line (JAX line 007909) and the resulting PV-Cre x Ai9 mice were back crossed to FVB WT and *Fmr1 KO* mice for 8 generations. All mice were housed in a vivarium with a 12-h light-dark cycle. Experiments were performed during the light cycle. Animals were weaned at P21-22 and afterward housed with up to five mice per cage. Before P21, pups were housed with their dam. The FVB background was chosen because of its robust breeding, and because the FVB *Fmr1* KO phenotype includes a predisposition to audiogenic seizures (Bernardet and Crusio, 2006). Due to the potentially stressful effects of surgeries on pups of early prenatal ages and their dams, homozygous litters were used to maximize survival by eliminating the possibility of littermates with different genotypes receiving unequal attention from the dam.

P1 injection of AAV vector for GCaMP6s expression in primary somatosensory cortex (S1)

rAAV (AAV1.Syn.GCaMP6s.WPRE.SV40) (Chen et al., 2013) was purchased from the University of Pennsylvania Vector Core and diluted to a working titer of 2E13 with 1% filtered Fast Green FCF dye. Pups were anesthetized with isoflurane (5% induction, 1.5-2% maintenance via a nose cone, volume-to-volume) and placed in a stereotaxic frame. A subcutaneous injection of Carprofen (Rimadyl, Pfizer; 5 mg/kg) was administered. The scalp was sterilized with alternating swabs of betadine and 70% alcohol. A small skin flap (2-3 mm in length) was made over the somatosensory cortex. The periosteum was gently cleared under the skin flap using brief, gentle touches of a dental drill. At the injection site, the bone was drilled lightly to create a small crack, permitting injection via pulled-glass capillary without exposing the dura. Glass micropipettes (Sutter Instrument, 1.5 mm outer diameter, 0.86 mm inner diameter) were used to inject approximately 0.2 μL of rAAV into the superficial cortex at a depth of 0.2 mm below the dura, using a Picospritzer (General Valve) (**Fig. 9a** left). After removing the pipette, the injection site was sealed with a small drop of VetBond (3M). The skin flap was replaced and the skin edges were sealed with VetBond. The entire surgery was completed in 15-20 min per animal. The pup was allowed to recover on a warm water circulation blanket before being returned to the dam.

Cranial window surgery for P14-16 imaging in S1

Pups (P10-12) were anesthetized with isoflurane (5% induction, 1.5-2% maintenance via a nose cone, vol/vol) and placed in a stereotaxic frame. A 2.5-3.5 mm diameter craniotomy was performed over the right barrel cortex and covered with a 3 or 5 mm glass coverslip, as previously described

(Golshani and Portera-Cailliau, 2008, Mostany and Portera-Cailliau, 2008). A headbar was also attached to the skull with dental cement to secure the animal to the microscope stage. The cranial window surgery itself can be done in under 60 min, and our protocol and custom headbars were designed to facilitate postoperative reintegration into the litter. Within 2 hours after surgery the pups appeared fully recovered from the effects of anesthesia and were able to nurse normally.

Cranial window surgery with AAV vector injection for adult GCaMP6s in S1

For 8 of the 10 WT adult animals and 5 of the 8 *Fmr1* KO adult animals imaged, the AAV1.Syn.GCaMP6s.WPRE.SV40 vector was injected into the barrel cortex during the cranial window surgery, 2+ weeks before imaging, following existing protocols (Chen et al., 2013). After drilling a 4 mm craniotomy over the right barrel cortex, approximately 30 nL of rAAV vector, diluted to a working titer of 2E13 with 1% filtered Fast Green, was injected into 4-7 sites in the barrel cortex. The craniotomy was covered with a 5 mm glass coverslip, and a headbar was also attached to the skull with dental cement.

The remaining 2 WT adult animals and 1 of the remaining KO animals had been injected with rAAV vector at P1 and received cranial window implantation at P10-12, following the previously described protocol, but were not used for the P14-16 imaging experiments. The remaining 2 of 8 KO adult animals had been injected with rAAV vector at P1, had received cranial window implantation at P10-12, and had also been used for the P14-16 imaging experiments.

Cranial window surgery for primary visual cortex (V1)

Experiments were started with craniotomies performed at 6-8 weeks on the four different mouse lines mentioned above. Mice were anesthetized with isoflurane (5% induction, 1.5-2% maintenance via a nose cone) and placed in a stereotaxic frame. A 4.5 mm diameter craniotomy was performed over the right primary visual cortex (V1) and covered with a 5 mm glass coverslip, as previously described (Golshani and Portera-Cailliau, 2008, Mostany and Portera-Cailliau, 2008). Before securing the cranial window with a coverslip, we injected ~50 nl of AAV1.Syn.GCaMP6s.WPRE.SV40 (**Fig. 13a**, in vivo calcium imaging of L2/3 pyramidal neurons), or a cocktail of AAV1.Syn.GCaMP6s.WPRE.SV40 and AAV1.Syn.Flex.GCaMP6s.WPRE.SV40 (**Fig. 14**, *in vivo* calcium imaging in PV cells), or a cocktail of AAV1.Syn.Flex.GCaMP6s.WPRE.SV40 and pAAV.hSyn.DIO.hM3D(Gq).mCherry **(Fig. 15**, to activate PV cells with DREADDs). A custom U-shaped aluminum bar was attached to the skull with dental cement to head restrain the animal during behavior and calcium imaging.

Optical Intrinsic Signal (OIS) imaging in S1

Following cranial window surgery, OIS imaging was used to map the barrel cortex at P12-14 (for P14-16 imaging) or at least 1 day before imaging (for adults). As previously described (Johnston et al., 2012), the contralateral whisker bundle was gently attached using bone wax to a glass needle coupled to a piezo-actuator (Physik Instrumente). Each stimulation trial consisted of a 100 Hz sawtooth stimulation lasting 1.5 s. The response signal divided by the averaged baseline signal,

summed for all trials, was thresholded at a fraction (65%) of maximum response to delineate the cortical representation of stimulated whiskers (**Fig. 9b**). OIS signal intensities were not quantified, nor were they compared between animals.

Optical Intrinsic Signal (OIS) imaging in V1

Two weeks after cranial window surgery, OIS imaging was used to map the location of V1. Visual stimulation was provided by a piezo-actuator (Physik Instrumente) that deflected light from a red light emitting diode in front of the contralateral eye. The response for 30 stimulation trials was averaged, each consisting of 100 Hz deflections for 1.5 s. The response signal divided by the averaged baseline signal, summed for all trials, was used to generate the visual cortical map.

***In vivo* two-photon calcium imaging in head-restrained mouse S1**

Calcium imaging was performed on a custom-built two-photon microscope, with a Chameleon Ultra II Ti:sapphire laser (Coherent), a 20X objective (0.95 NA, Olympus) and ScanImage software (Pologruto et al., 2003). Mice were lightly sedated with chlorprothixene (2 mg/kg, i.p.) and isoflurane (0-0.5%), and kept at 37°C using a temperature control device and heating blanket (Harvard Apparatus). The isoflurane was manually adjusted to maintain a breathing rate ranging from 100-150 breaths/min for P14-16 mice and 140-150 breaths/min for adult mice. Both spontaneous activity and whisker-evoked barrel cortex activity were recorded. Whisker stimulation was delivered by bundling the contralateral whiskers (typically all macrovibrissae of

at least ~1 cm in length), via soft bone wax, to a glass needle coupled to a piezo-actuator (**Fig. 9a** right). The stimulation protocol was the same as that used during behavioral experiments (**Fig. 9d**). Whole-field images were acquired at 7.8 Hz (1024 x 128 pixels downsampled to 256 x 128 pixels) (**Fig. 9c**).

***In vivo* two-photon calcium imaging in head-restrained mouse V1**

Following rig habituation, mice were introduced to the visual stimuli on the screen. This stimulus habituation phase lasted 3-4 sessions. Visual stimuli were generated using custom-written MATLAB (Mathworks) routines using Psychtoolbox that consisted of full-field square wave drifting gratings (2 cycles/s, 0.005 spatial frequency, 32 random repeats of 8 orientations) presented for 3 s and separated by a 3 s-long grey screen. Both spontaneous and visually evoked responses of L2/3 pyramidal cells from V1 were recorded at 15 Hz in 2-4 fields of view. Each FOV consisted of a median of 63 pyramidal cells (range: WT=54-81; *Fmr1 KO* = 57-79) or 8 PV cells (range: WT=3-10; *Fmr1 KO* = 3-8). In each animal, imaging was performed at 2-3 depths (150-250 μm), and data was averaged from movies collected across all FOVs.

Data analysis for calcium imaging in S1

Calcium-imaging data were analyzed using EZcalcium (see Chapter I). In 4 out of 20 movies of P14-16 spontaneous activity (1,600 frames acquired), between 8 and 34 frames with significant Z-motion were manually removed before motion correction. In 1 out of 20 movies of P14-16 evoked

activity (800 frames), 24 frames with Z-motion occurred during the initial 10 seconds of baseline acquisition before whisker stimulation began, allowing replacement of these frames with an averaged Z-projection of the remainder of the video. In 11 out of 20 movies of P34-74 spontaneous activity (1,600 frames acquired), some frames (up to 420) exhibiting Z-axis motion were manually removed before motion correction. Subsequent data quantifications used only the first 800 frames of spontaneous activity, i.e., an equivalent duration as the evoked activity.

X-Y drift in the movies was then corrected using either a frame-by-frame, Hidden-Markov-Model-based registration routine (Dombeck et al., 2007) or a cross-correlation-based, non-rigid alignment algorithm (Mineault et al., 2016). The choice of registration algorithm did not affect the data analysis, since the fluorescence data for each neuron was always normalized to its own baseline. A semi-automated algorithm (Chen et al., 2013) was used to select regions of interest, each representing a single cell body, and extract the fluorescence signal ($\Delta F/F$) for each neuron. A "modified Z-score" Z_F vector for each neuron was calculated as

$$Z\_F = \frac{F(t) - mean(quietest\ period)}{std(quietest\ period)}$$

where the quietest period is the 10 s period with the lowest variation (standard deviation) in $\Delta F/F$. All subsequent analyses were performed using the Z_F vectors.

To define whether an individual cell showed time-locked responses to whisker stimulations (**Fig. 9g-h and 11b**), a probabilistic bootstrapping method was implemented. First, we calculated the

correlation between the stimulus time-course and the Z_F vector, followed by correlation calculations between the stimulus time-course and 10,000 scrambles of all calcium activity epochs in Z_F (epoch = consecutive frames wherein Z_F ≥ 3). The 10,000 comparisons generated a distribution of correlations (R values), within which the correlation of the unscrambled data and the stimulus fell at a certain percentile. If the calculated percentile for a cell was less than 0.01, then we described that cell as being time-locked.

For analysis of aggregate activity within a particular time range, as in **Figs. 9f**, **10d-f**, **11a**, or **11c-e**, the mean of Z_F within that time range was calculated for each ROI, and for each animal imaged, a median Z_F was then calculated across all ROIs or a subset of ROIs (e.g. only time-locked or non-time-locked ROIs). The initial and end baseline periods of Evoked activity were included in the analyses for **Figs. 9f, 9h,** and **11a-b**.

For curve fitting of WT neuronal activity across stimulations (**Fig. 10c**), we calculated the median Z_F across ROIs for each animal imaged, within each of the 20 stimulations (from 0.2 s before stimulation onset to 2.8 s after stimulation end), and then applied iterative nonlinear, least-squares curve fitting with the Levenberg-Marquardt algorithm. The best-fit exponential curve to all data points for each stimulation had the equation $y = Ae^{-x/\tau} + off$, where A = 1.94±0.25, τ = 4.10±1.26, and *off* = 1.42±0.14.

To analyze the correlation between the WT and *Fmr1 KO* animals' proportions of time-locked neurons and their respective Adaptation Index of activity (**Fig. 10g**), we calculated an Adaptation Index as:

$$\frac{(Z\ score\ during\ First\ 5\ stimulations) - (Z\ score\ during\ Last\ 5\ stimulations)}{(Z\ score\ during\ First\ 5\ stimulations) + (Z\ score\ during\ Last\ 5\ stimulations)}$$

Statistical analyses

Central tendencies are reported in the main text as group median ± median absolute deviation. Graphs show all data points as well as group medians and, where error bars are shown, interquartile ranges. Based on our group sizes of n=8-10 for imaging data comparisons and n=13-21 for behavioral data comparisons, normality cannot be ensured, and tests of normality and variance are also unreliable. As such, we implemented a conservative statistical approach of all rank-based comparisons with bootstrapping (10,000 resamples), without assumptions regarding normality or variance. These comparisons were implemented using custom-written R code. Paired rank-based comparisons were used when comparing measurements within the same animals (e.g. median fluorescence Z-scores during the first five vs. last five stimulations in WT mice). Unpaired rank-based comparisons were used when comparing measurements in different animals (e.g. % time-locked neurons in WT vs. *Fmr1* KO mice). Two-sided p-values were calculated for each comparison, and Bonferroni corrections for multiple comparisons were applied where appropriate. The threshold for significance was set at $p<0.05$.

No statistical test was used to prospectively calculate sample sizes. Target sample sizes were based on previous work from our group (Golshani et al., 2009, Goncalves et al., 2013), and equal or exceed sample sizes for other recent studies using *in vivo* calcium imaging and head-fixed

behavior. Experimenters were aware of the genotype of the animals in each experiment, as homozygous litters were used. Both male and female animals were used.

Data analysis for calcium imaging in V1

Orientation selective cells were defined by an orientation selectivity index (OSI) calculated as

$OSI=(Zpref-Zorth)(Zpref+Zorth)$OSI=(Zpref−Zorth)(Zpref+Zorth)

where *Zorth* is the mean response to the orientation orthogonal to the preferred one (*Zpref*). A cell was considered orientation-selective if it had OSI ≥ 0.5.

To quantify visually evoked activity, we averaged the responses of neurons during the 3 s of drifting gratings stimulation and the 3 s of gray screen that followed the visual stimulus. To quantify spontaneous activity, we conducted separate recordings during which the animals were presented a static gray screen. To determine whether an individual cell showed a time-locked or stimulus-selective response to a visual stimulus in Fig. 13 (which examines the correlation between the stimulus and the fluorescence signal in PV cells), we used a probabilistic bootstrapping method as described previously. First, we calculated the correlation between the stimulus time-course and the Z_f vector, followed by correlation calculations between the stimulus time-course and 1,000 scrambles of all calcium activity epochs in Z_f (epoch = consecutive frames wherein $Z_f \geq 3$). The 1,000 comparisons generated a distribution of correlations (*r* values), within which the correlation of the unscrambled data and the stimulus fell at any given percentile. If the

calculated percentile for a cell was less than 1%, then we described that cell as being stimulus selective. Correlations in Figs. 13 and 15j were calculated using a Pearson's correlation.

Our tuning width calculation procedures are similar to what has been described before. First, we generate a tuning curve of the mean *z*-score values of the responses for each orientation presented. The orientation with the largest mean response is considered the preferred orientation. A Gaussian is then fitted to the tuning curve, and the tuning width is determined to be the width at half the maximum value of the fitted Gaussian. The equation of the Gaussian we use is the one used in Akerboom et al.

$$\sigma \cdot 2 \cdot \ln 2 \text{−−−−−} \sqrt{\sigma \cdot 2 \cdot \ln f_0 2}$$

We included only neurons that elicited at least one calcium transient during the duration of the recording; neurons were excluded if they were deemed inactive on the basis of calcium imaging data (pyramidal neurons excluded: WT = 0.1%; *Fmr1*$^{-/-}$ = 0.1%; PV neurons excluded: WT = 0.1%; *Fmr1*$^{-/-}$ = 0.1%).

Transcardial perfusion and DiI histology

Mice were deeply anesthetized with isoflurane and underwent transcardial perfusion with 4% paraformaldehyde solution in sodium phosphate buffer (composition: 30 mM NaH_2PO_4, 120 mM Na_2HPO_4, pH 7.4). Brains were kept overnight at 4 °C first in 4% paraformaldehyde solution (pH 7.4) and then stored in 30% sucrose (in phosphate buffered saline) at 4 °C until sectioned.

Human subjects

Eight male with FXS and eight male healthy controls, matched in chronological age, completed the visual discrimination experiment. Testing was conducted at a regional academic pediatric medical center where the participants with FXS were originally recruited as part of our Center for Collaborative Research in Fragile X (U54). Approval of this study was granted through the Institutional Review Board at Cincinnati Children's Hospital Medical Center. All participants > 18 years of age provided written consent, and minors provided assent plus written consent from their legal guardians. Additional consent was obtained to use the de-identified photograph of an FXS participant performing the task. All FXS participants had full *FMR1* mutations (> 200 CGG repeats) confirmed by genetic testing. No participants had a history of nonfebrile seizures or treatment with an anticonvulsant medication. FXS participants completed the Abbreviated Battery of the Stanford-Binet Intelligence Scales-Fifth Edition (SB-5). Control participants were recruited through hospital-wide and community advertisements and were excluded for a history of developmental or learning disorders or significant psychiatric disorder (for example, schizophrenia) in themselves or in first degree-relatives, or for a family history of ASD in first- or second-degree relatives based on a brief screening interview. All study procedures were approved by the local Institutional Review Board.

Human FXS and control participants completed a visual discrimination task that was analogous to the one used with mice, with relatively minor modifications. Due to the additional cognitive demands of a go/no-go experiment, including inhibitory control, which is known to be impaired in FXS, we designed a forced two-choice visual discrimination task, so that all FXS participants

could learn and perform the task in a single session. It is conceivable, however, that FXS subjects could have learned the go/no-go task with subsequent training sessions, just as the mice required consecutive sessions to learn; however, time constraints and burden on the patient population limited our ability to do so. Visual gratings were displayed on a 13-inch (33.02-cm) Hewlett Packard laptop computer with a 15-inch (38.1-cm) liquid crystal display and made responses by pressing designated keys on the laptop keyboard. During the task, when the visual grating appeared to move from right side to left side, subjects were instructed to press the corresponding left-side key ('Z' or 'A'), and when the visual grating appeared to move from left to right, subjects were instructed to press the corresponding right-side key ('L' or 'M'). If participants correctly responded to the direction of the stimulus, they received positive visual feedback (for example, images of popular video game cartoon characters were displayed on the computer screen). If participants incorrectly responded to the direction of the stimulus, they received negative visual feedback (for example, a large red 'X' was displayed). Visual gratings appeared on screen for 4 s, during which participants could respond. Once the participant responded or at the end of 4 s, feedback was presented for 1 s. The following trial would begin 3 s later. All participants completed the first-order visual task, followed immediately by the second-order visual task. For each of the tasks, visual gratings appeared in four blocks of 30 trials, each block consisted of one condition: 180°/0°, 45°/90°, 67.5°/45°, or 82.5°/15°. The order of the blocks was presented randomly, but participants always received first-order blocks before second-order. Prior to administration of the task, participants completed two practice blocks. During the first practice block, a smiley face emoji moved from left to right on the screen (or right to left), and participants were instructed to press the corresponding key based on the direction the smiley

faced moved. In the second block, visual gratings at 50°/80° angles were presented, and participants pressed the key corresponding to direction of movement. Twelve trials of each practice block were administered. If participants did not reach ≥50% correct trials, the block was repeated one time for a total of 24 trials per block. All participants met practice criterion. Depending on the stimulus presented, the subject's behavioral response was characterized as 'Right' (similar to Hit), 'NR' (no response) or 'Wrong' (similar to FA). Since this was a two-choice forced visual discrimination task, a modified d' (discriminability index) was calculated as follows:

d'=norminv(fractionofRight)−norminv(fractionofWrong)d′=norminv(fractionofRight)−norminv(fractionofWrong)

Statistical analysis

Statistical analysis of normality (Lilliefors and Shapiro–Wilk tests) were performed on each dataset and, depending on whether the data significantly deviated from normality ($P < 0.05$) or did not deviate from normality ($P > 0.05$), appropriate nonparametric or parametric tests were performed. The statistical tests performed are mentioned in the text and the legends. For parametric two-group analyses, a Student's t test (paired or unpaired) was used. For nonparametric tests, we used the following: Mann–Whitney test (two groups), Kruskal–Wallis test (three or more groups), and Friedman test (repeated measures). In the figures, significance levels are represented with the following convention: $*P < 0.05$; $**P < 0.01$, $***P < 0.005$. In all figures, we plot the s.e.m. Graphs show either individual data points from each animal or group means (averaged over different mice) superimposed on individual data points.

Sample size

We did not use statistical methods to predetermine sample sizes. For all main results shown in Figs. 2-3, we used sample sizes of ≥ 10 mice, and subsequent statistics were performed using the number of mice as the sample size. Working with *Fmr1*$^{-/-}$ mice can be technically challenging for several reasons: (i) *Fmr1*$^{-/-}$ mothers have a higher incidence of cannibalization, (ii) *Fmr1*$^{-/-}$ mice can require extra handling to habituate them to any behavioral task, and extra care is required during water deprivation because a fraction of them can show adverse effects such as excessive weight loss, which could lead to seizures. Hence, to maintain the feasibility of experiments and ethical use of numbers of animals for most of our experiments, we used at least 10 mice per group.

In Figs. 14 and 15 we used triple transgenic mice: PV-Cre mice were crossed with Ai9 mice and these were then back crossed to FVB WT and *Fmr1* $^{-/-}$ mice for eight generations. Generation of a triple transgenic line was time-consuming and resource-intensive, and we faced the same technical challenges associated with using *Fmr1*$^{-/-}$ mice; hence, we used $n \geq 6$ mice. Again, statistics were performed using the number of mice as the sample size.

The sample size we used is consistent with those in previously published studies. For the inactivation of visual cortex experiments (**Fig. 11c**), the sample size was in agreement with previous studies. For Fig. 16 we used $n = 8$ humans for each group. Recruiting age- and gender-matched patients with Fragile X syndrome is challenging, but a sample of 8 per group is comparable to the number of human subjects used in previously published studies.

Randomization

We ensured that during a behavior training cycle, both WT and *Fmr1*$^{-/-}$ were included to exclude any biases introduced by experimenters or the training rig. Similarly, on a particular testing day, subjects with Fragile X syndrome were randomized with control subjects.

Discussion

Creating an accessible and adaptable toolbox for analysis of calcium imaging data

The main goal of my thesis was to develop a complete toolbox for analysis of calcium imaging data that could be freely disseminated across the scientific community. Our main priority was that the toolbox be easy to use and compatible with different types of calcium imaginf. We accomplished this by implementing simple and intuitive GUIs that provide a 'push-button' feel for the user. Next, we wanted it to be comprehensive, meaning that it would accomplish the main steps that most users would require, namely registration (achieved by the Motion Correction module), segmentation and signal extraction(achieved by the ROI Selection and ROI Refinement modules). For these steps, we incorporated the latest MATLAB resources for analysis of calcium imaging data (Vogelstein et al., 2010, Mineault et al., 2016, Pnevmatikakis et al., 2016). Finally, we intended for EZcalcium to be flexible, so that different users could eventually add new capabilities to it. In order for investigators in various fields to get a sense of its full capabilities, we presented examples of different types of imaging (axon boutons, somatic signals with two-photon and miniscope imaging, and drosophila projections).

All three major components of EZcalcium (Motion Correction, ROI Detection, and ROI Refinement) are fundamental steps in the processing of dynamic fluorescence signals in biology. Although we designed EZcalcium primarily with calcium imaging in mind, the toolbox should in principle be compatible with other types of dynamic fluorescence data, such as voltage indicators (Antic and Zecevic, 1995) and neurotransmitter sensors (Marvin et al., 2013). The underlying process involving localized changes in fluorescence intensity indicative of biological activity is conserved across these different indicators and imaging parameters. The GUIs are also flexible

enough to be adapted for to these various tasks. Thus, EZcalcium is adaptable to novel fluorescent indicators other than calcium imaging.

By being open source and modular, our toolbox could readily be adapted and upgraded to specific needs and yet-to-be-conceived methods of detecting calcium signals by the scientific community. An example of a potential modification would be the ability to deconvolve a dF/F signal obtained from a fluorescent voltage indicator into a voltage signal after conducting experiments with simultaneous electrophysiology with fluorescent voltage imaging. Similarly, additional filters could be incorporated in the Motion Correction module for low-fidelity imaging, such as with head-mounted miniscopes or in order to remove artifacts that appear during certain forms of imaging that may results in a specific noise pattern, such as the presence of an LED or other light sources interfering with imaging.

Additional forms of data analysis can be easily incorporated for labs looking for a simple interface with which to perform all their analyses, such as population coupling (Okun et al., 2015) or correlation with a sensory stimulus (He et al., 2017, Goel et al., 2018). Furthermore, by making use of ROI centers that are currently exported as part of ROI Refinement, spatial relationships between ROIs that correlate with activity can also be examined, taking into account this distinct advantage that fluorescent imaging has over other methods of activity detection, such as silicon probe recordings.

The latest major calcium analysis toolbox is CaImAn (Giovannucci et al., 2019). Many of the algorithms available in EZcalcium were borrowed from CaImAn, and the modifications that we have made to algorithms written by the CaImAn team have now been submitted for incorporation into their open source software. Unfortunately, for the average inexperienced scientist, CaImAn would be considerably more difficult to use, with the majority of the development being targeted to Python programmers. While this may increase processing speed to a degree, it will greatly diminish its accessibility. Furthermore, it lacks an ROI refinement step to eliminate false-positives. We consider this to be a critical step because the ROI detection algorithms in CaImAn are prone to false-positives, especially when relying on fully-automated ROI selection.

Neural circuitry abnormalities underlying tactile defensiveness in Fmr1 KO mice

A common symptom in FXS that is also seen in other ASDs is sensory hypersensitivity, frequently manifesting as tactile defensiveness (Sinclair et al., 2017). Sensory overreactivity is significant because it can contribute to other symptoms, such as anxiety, sleep disturbances, seizures, and inattention, and disrupt activities of daily living. Clinical interventions to improve sensory modulation in ASDs rely on behavioral or pharmacological treatments that are not specific for the underlying disorder (van Karnebeek et al., 2016). Coinciding with the disappointments of recent clinical trials aimed at molecular targets (Mullard, 2015), neuroscientists are increasingly turning to *in vivo* recordings of network activity in rodent models of ASDs (Goncalves et al., 2013, Arnett et al., 2014, Zhang et al., 2014, Lu et al., 2016) to discover new therapeutic targets.

We followed such a symptom-to-circuit approach and designed our experiments to characterize circuit-level defects underlying sensory abnormalities in the *Fmr1* KO mouse model of FXS. We used *in vivo* calcium imaging with GCaMP6s to record ensemble activity of L2/3 neurons in the barrel cortex and the primary visual cortex during stimulation. Our main results are as follows: 1) Adult KO mice show an avoidance response to repetitive whisker stimulation, resembling tactile defensiveness in FXS patients; 2) Unexpectedly, we found no evidence of exaggerated sensory-evoked neuronal activity in L2/3 of young or adult KO mice; 3) The proportion of L2/3 neurons in barrel cortex that responds in a time-locked manner to whisker stimulation is 45% lower in KO mice compared to WT mice at P14-16; 4) Neuronal activity in both young and adult KO mice shows a lack of adaptation to repetitive whisker stimulation; 5) Our results indicate that the absence of adaptation within local neuronal networks is a likely contributor to sensory overreactivity in FXS, and perhaps in other ASDs; 6) KO mice display impaired visual discrimination ability correlating with reduced orientation tuning; 7) PV interneurons play a key role in learning and performance of a visual discrimination task and may be a strong candidate for therapeutics; 8) Clinical applicability is supported as humans with FXS display similar defects on a visual discrimination task as shown in KO mice.

For our somatosensory experiments we chose to stimulate groups of whiskers to better mimic the passive whole-snout inputs due to contact with littermates and grooming by the dam, which dominate the animals' early somatosensory experience. Our stimulation characteristics were also physiologically relevant, as exploratory whisking in mice is typically 5-15 Hz in 1-4 s bouts (Kleinfeld et al., 2006). Whereas each of our 20 stimulations (10 Hz for 1 s) was physiological in

intensity and duration, the repetitive nature of the entire 80 s stimulation series was chosen to be more akin to a environmental stimulation that might be persistently irritating (e.g., wearing certain clothes), without being shocking (e.g., a brief but extremely loud sound). Our results on neuronal adaptation to repetitive whisker stimulation in early postnatal WT mice are consistent with those of a recent study using multi-electrode array recordings (van der Bourg et al., 2017), in which barrel cortex activity in young mice was recorded during 10 consecutive 10 ms-long whisker deflections (200 ms ISI). It is important to note that the time course of stimulation and adaptation we chose is particularly relevant to studying the problem of tactile defensiveness in autism.

In adult mice, brief (200 ms) deflections of 2-3 whiskers cause inter-whisker inhibition between barrel cortex neurons within <500 ms (Simons, 1985); conversely, during 10 Hz multi-whisker stimulations lasting 1 s, adaptation of barrel cortex neurons enables "surround facilitation" instead of suppression (Ramirez et al., 2014). As we examined adaptation over much longer time scales, it is unlikely that single-whisker stimulation would reveal different results (we find that single-whisker stimulation also leads to neuronal adaptation in WT mice; not shown). One caveat regarding the interpretation of our results is that we imaged L2/3 activity in barrel cortex of lightly sedated mice, in order to maintain a consistent behavioral state, as well as to minimize active whisking events that might contribute to feedback-enhanced cortical activity and contaminate our recordings (Petersen, 2007). While deep anesthesia (>1% isoflurane) is known to produce a markedly different neuronal activity pattern from the awake state, light (<0.5%) isoflurane allows a sparse, desynchronized pattern of neuronal population activity that is similar to the awake state (Lissek et al., 2016).

We unexpectedly found that the proportion of L2/3 neurons showing time-locked responses to whisker stimulation was much lower in *Fmr1* KO than in WT animals at P14-16 (though not evident in adult mice), and that sensory stimulation did not trigger abnormally high activity in neurons from KO mice at either age. This seems to contradict predictions of the theory of neuronal and network hyperexcitability in FXS (Contractor et al., 2015). However, the L2/3 activity from single whisker stimulation is distributed across several cortical columns, with only 25% of excitatory neurons in a single imaging field showing responses tuned to the anatomically associated whisker (Clancy et al., 2015). It is possible that in KO mice the functional circuits for whisker touch processing are dispersed over an even larger spatial area, resulting in an apparently reduced proportion of time-locked neurons within any given local network (about 200 μm in diameter), as we observed. Indeed, recent studies using OIS and *in vivo* electrophysiology found that single whisker stimulation resulted in a larger spatial area of activation across the *Fmr1* KO barrel cortex, compared with WT (Arnett et al., 2014, Juczewski et al., 2016).

Adaptation of cortical neurons to repeated or ongoing sensory stimulation is a robust phenomenon across sensory modalities, enabling increased detection and discriminability (Castro-Alamancos, 2004, Ollerenshaw et al., 2014). Given our results, *Fmr1* KO mice would be expected to show impairments in behavioral tasks that assess tactile perception and perceptual decision-making. Indeed, these mice have demonstrated impaired texture discrimination during novel object recognition (Orefice et al., 2016), as well as reduced whisker sampling (Juczewski et al., 2016) and impaired learning (Arnett et al., 2014) in the gap-crossing assay.

We speculate that altered sensory processing in the cortex might lead to anxiety and hyperarousal and ultimately contribute to the observed defensiveness behavior in *Fmr1* KO mice. Our data fit well with not just the known behavioral phenotypes of KO mice and FXS patients, but also with existing EEG studies on sensory adaptation defects in KO mice and humans (Castren et al., 2003, Van der Molen et al., 2012, Ethridge et al., 2016, Sinclair et al., 2017, Lovelace et al., 2018). A recent fMRI study also found a defect in adaptation to repeated tactile stimulus in the somatosensory cortex of patients (age 9-17) with both ASD and documented sensory overreactivity (Green et al., 2015). Our work encourages additional investigations using animal models of ASD at developmental stages to elucidate neuronal defects underlying aberrant behaviors that are relevant to human symptoms and function.

Neural circuitry defects underlying impaired visual discrimination in *Fmr1* KO mice

Progress in FXS research is limited by the lack of clearly identified circuit-level alterations that can explain the neuropsychiatric phenotype that characterizes the disorder. Though circuit activity in monogenetic murine models of autism can be readily interrogated and manipulated, there is increasing interest to demonstrate both face validity and predictive validity for these translational approaches to be used in clinical trials (Robertson and Baron-Cohen, 2017). To bridge this gap, we implemented a fully translatable behavioral assay of perceptual learning and discrimination in both *Fmr1 KO* mice and FXS patients and followed a symptom-to-circuit approach to delineate specific circuit-level defects using calcium imaging in V1. Our discovery that *Fmr1 KO* mice have a reduced proportion of orientation selective neurons with abnormally broad tuning in V1, as

well as extremely hypoactive PV cells, provides a mechanistic understanding of their visual discrimination deficits. The fact that we could rescue the perceptual deficits in mice by restoring activity in PV cells with DREADDs and that humans with FXS exhibit analogous deficits in visual discrimination, provides a realistic path for novel translational clinical trials.

Our data implicates a role for PV cells in circuit dysfunction in FXS through converging evidence of their hypoactivity from experiments in two different groups of mice (*Fmr1 KO* and *Fmr1 KO*^{hM3Dq}), and from the DREADD approach, which not only restored PV cell activity, but also raised the percentage of orientation selective pyramidal cells in V1. But additional studies will be necessary to fully elucidate the role of PV cells in network dysfunction in FXS, at least in part because their influence on the circuit is rather complex and likely depends on the level and duration of their engagement in a given computation (Atallah et al., 2012). Moreover, it is also possible that suppressed activity of PV neurons might paradoxically lead to an increase in inhibitory synaptic input to L2/3 ("network suppression) as recently described in auditory cortex (Kato et al., 2017).

It is exciting to consider that PV cell dysfunction could be involved in other aspects of FXS, such as impaired neuronal adaptation in tactile defensiveness (He et al., 2017). Additionally, by rapidly translating this paradigm into a clinical population, we have substantially reduced potential barriers to further study whether PV cell dysfunction represents an important aspect (or even the principal one) of a *canonical micro-circuitry* in autism (Robertson and Baron-Cohen, 2017). In the future, the pilot human FXS data will need to be bolstered by further studies with additional subjects that

1) incorporate a visual evoked potential study to clarify the contribution, if any, of visual processing abnormalities to the task results and 2) evaluate more extensively the degree of visual learning deficits prior to the reduction in discriminability.

Running is known to have an impact on visually evoked activity of both excitatory and inhibitory neurons in V1 (Niell and Stryker, 2010, Pakan et al., 2016). Nevertheless, because we did not observe any differences in the magnitude of running between genotypes, we cannot attribute the deficits of *Fmr1 KO* mice in visual discrimination or their altered network activity to locomotion. The lack of changes in spontaneous neuronal activity in V1 of *Fmr1 KO* mice, together with the fact that we could manipulate the gain of PV cell output to restore circuit function and rescue behavior, highlights the important notion that perhaps the basal circuit connectivity remains 'intact' in adult *Fmr1 KO* mice. However, depending on the computational demands imposed by sensory environment, *Fmr1 KO* mice are unable to efficiently process sensory information, which impairs their ability to properly utilize this information to perform a task. Thus, simple therapeutic strategies that target relatively subtle circuit level alterations that are specific to different behavioral impairments may be of value in autism.

In summary, for my Ph.D. thesis I first developed new tools for analyzing neural activity data and made these not only freely available, but also accessible and applicable for current and future scientists without the need for a dedicated programmer or computational neuroscientist. Secondly, I contributed to the field of FXS research by investigating the circuit mechanisms of atypical sensory processing. I hope that my research serves an example of how to incorporate the

investigation and probing of neural circuits in a symptoms-to-circuit approach that makes use of powerful emerging imaging technologies to improve research.

References

Aharoni D, Khakh BS, Silva AJ, Golshani P (2019) All the light that we can see: a new era in miniaturized microscopy. Nature methods 16:11-13.

Akerboom J, Carreras Calderon N, Tian L, Wabnig S, Prigge M, Tolo J, Gordus A, Orger MB, Severi KE, Macklin JJ, Patel R, Pulver SR, Wardill TJ, Fischer E, Schuler C, Chen TW, Sarkisyan KS, Marvin JS, Bargmann CI, Kim DS, Kugler S, Lagnado L, Hegemann P, Gottschalk A, Schreiter ER, Looger LL (2013) Genetically encoded calcium indicators for multi-color neural activity imaging and combination with optogenetics. Frontiers in molecular neuroscience 6:2.

Andermann ML, Kerlin AM, Reid RC (2010) Chronic cellular imaging of mouse visual cortex during operant behavior and passive viewing. Frontiers in cellular neuroscience 4:3.

Antic S, Zecevic D (1995) Optical signals from neurons with internally applied voltage-sensitive dyes. The Journal of neuroscience : the official journal of the Society for Neuroscience 15:1392-1405.

Armbruster BN, Li X, Pausch MH, Herlitze S, Roth BL (2007) Evolving the lock to fit the key to create a family of G protein-coupled receptors potently activated by an inert ligand. Proceedings of the National Academy of Sciences of the United States of America 104:5163-5168.

Arnett MT, Herman DH, McGee AW (2014) Deficits in tactile learning in a mouse model of fragile X syndrome. PloS one 9:e109116.

Atallah BV, Bruns W, Carandini M, Scanziani M (2012) Parvalbumin-expressing interneurons linearly transform cortical responses to visual stimuli. Neuron 73:159-170.

Bagni C, Zukin RS (2019) A Synaptic Perspective of Fragile X Syndrome and Autism Spectrum Disorders. Neuron 101:1070-1088.

Bakker C, Verheij V, Willemsen R, Helm Rvd, Oerlemans F, Vermey M, Bygrave A, Hoogeveen A, Oostra B, Reyniers E, Boule KD, D'Hooge R, Cras P, Velzen Dv, Nagels G, Martin J, Deyn PD, Darby J (1994) Fmr1 knockout mice: a model to study fragile X mental retardation. The Dutch-Belgian Fragile X Consortium. Cell 78:23-33.

Belmonte MK, Allen G, Beckel-Mitchener A, Boulanger LM, Carper RA, Webb SJ (2004) Autism and abnormal development of brain connectivity. The Journal of neuroscience : the official journal of the Society for Neuroscience 24:9228-9231.

Ben-Sasson A, Cermak SA, Orsmond GI, Tager-Flusberg H, Carter AS, Kadlec MB, Dunn W (2007) Extreme sensory modulation behaviors in toddlers with autism spectrum disorders. The American journal of occupational therapy : official publication of the American Occupational Therapy Association 61:584-592.

Bernardet M, Crusio WE (2006) Fmr1 KO mice as a possible model of autistic features. ScientificWorldJournal 6:1164-1176.

Butler MG, Mangrum T, Gupta R, Singh DN (1991) A 15-item checklist for screening mentally retarded males for the fragile X syndrome. Clinical genetics 39:347-354.

Castren M, Paakkonen A, Tarkka IM, Ryynanen M, Partanen J (2003) Augmentation of auditory N1 in children with fragile X syndrome. Brain Topogr 15:165-171.

Castro-Alamancos MA (2004) Absence of rapid sensory adaptation in neocortex during information processing states. Neuron 41:455-464.

Chen TW, Wardill TJ, Sun Y, Pulver SR, Renninger SL, Baohan A, Schreiter ER, Kerr RA, Orger MB, Jayaraman V, Looger LL, Svoboda K, Kim DS (2013) Ultrasensitive fluorescent proteins for imaging neuronal activity. Nature 499:295-300.

Chung K, Wallace J, Kim SY, Kalyanasundaram S, Andalman AS, Davidson TJ, Mirzabekov JJ, Zalocusky KA, Mattis J, Denisin AK, Pak S, Bernstein H, Ramakrishnan C, Grosenick L, Gradinaru V, Deisseroth K (2013) Structural and molecular interrogation of intact biological systems. Nature 497:332-337.

Clancy KB, Schnepel P, Rao AT, Feldman DE (2015) Structure of a single whisker representation in layer 2 of mouse somatosensory cortex. The Journal of neuroscience : the official journal of the Society for Neuroscience 35:3946-3958.

Contractor A, Klyachko VA, Portera-Cailliau C (2015) Altered Neuronal and Circuit Excitability in Fragile X Syndrome. Neuron 87:699-715.

Dana H, Chen TW, Hu A, Shields BC, Guo C, Looger LL, Kim DS, Svoboda K (2014) Thy1-GCaMP6 transgenic mice for neuronal population imaging in vivo. PloS one 9:e108697.

Denk W, Strickler JH, Webb WW (1990) Two-photon laser scanning fluorescence microscopy. Science (New York, NY) 248:73-76.

Dombeck DA, Khabbaz AN, Collman F, Adelman TL, Tank DW (2007) Imaging large-scale neural activity with cellular resolution in awake, mobile mice. Neuron 56:43-57.

Ernst OP, Sanchez Murcia PA, Daldrop P, Tsunoda SP, Kateriya S, Hegemann P (2008) Photoactivation of channelrhodopsin. The Journal of biological chemistry 283:1637-1643.

Ethridge LE, White SP, Mosconi MW, Wang J, Byerly MJ, Sweeney JA (2016) Reduced habituation of auditory evoked potentials indicate cortical hyper-excitability in Fragile X Syndrome. Transl Psychiatry 6:e787.

Farzin F, Whitney D, Hagerman RJ, Rivera SM (2008) Contrast detection in infants with fragile X syndrome. Vision Res 48:1471-1478.

Fischl B (2012) FreeSurfer. NeuroImage 62:774-781.

Foster DJ, Conn PJ (2017) Allosteric Modulation of GPCRs: New Insights and Potential Utility for Treatment of Schizophrenia and Other CNS Disorders. Neuron 94:431-446.

Frye CG, MacLean JN (2016) Spontaneous activations follow a common developmental course across primary sensory areas in mouse neocortex. Journal of neurophysiology 116:431-437.

Gibson JR, Bartley AF, Hays SA, Huber KM (2008) Imbalance of neocortical excitation and inhibition and altered UP states reflect network hyperexcitability in the mouse model of fragile X syndrome. Journal of neurophysiology 100:2615-2626.

Giovannucci A, Friedrich J, Gunn P, Kalfon J, Brown BL, Koay SA, Taxidis J, Najafi F, Gauthier JL, Zhou P, Khakh BS, Tank DW, Chklovskii DB, Pnevmatikakis EA (2019) CaImAn an open source tool for scalable calcium imaging data analysis. eLife 8.

Goel A, Cantu DA, Guilfoyle J, Chaudhari GR, Newadkar A, Todisco B, de Alba D, Kourdougli N, Schmitt LM, Pedapati E, Erickson CA, Portera-Cailliau C (2018) Impaired perceptual learning in a mouse model of Fragile X syndrome is mediated by parvalbumin neuron dysfunction and is reversible. Nature neuroscience 21:1404-1411.

Golshani P, Goncalves JT, Khoshkhoo S, Mostany R, Smirnakis S, Portera-Cailliau C (2009) Internally mediated developmental desynchronization of neocortical network activity. The Journal of neuroscience : the official journal of the Society for Neuroscience 29:10890-10899.

Golshani P, Portera-Cailliau C (2008) In vivo 2-photon calcium imaging in layer 2/3 of mice. J Vis Exp.

Goncalves JT, Anstey JE, Golshani P, Portera-Cailliau C (2013) Circuit level defects in the developing neocortex of Fragile X mice. Nature neuroscience 16:903-909.

Gonchar Y, Burkhalter A (1997) Three distinct families of GABAergic neurons in rat visual cortex. Cerebral cortex (New York, NY : 1991) 7:347-358.

Green SA, Hernandez L, Tottenham N, Krasileva K, Bookheimer SY, Dapretto M (2015) Neurobiology of Sensory Overresponsivity in Youth With Autism Spectrum Disorders. JAMA Psychiatry 72:778-786.

Greenberg DS, Kerr JN (2009) Automated correction of fast motion artifacts for two-photon imaging of awake animals. Journal of neuroscience methods 176:1-15.

Hagerman RJ, Amiri K, Cronister A (1991) Fragile X checklist. American journal of medical genetics 38:283-287.

He CX, Arroyo ED, Cantu DA, Goel A, Portera-Cailliau C (2018) A Versatile Method for Viral Transfection of Calcium Indicators in the Neonatal Mouse Brain. Frontiers in neural circuits 12:56.

He CX, Cantu DA, Mantri SS, Zeiger WA, Goel A, Portera-Cailliau C (2017) Tactile Defensiveness and Impaired Adaptation of Neuronal Activity in the Fmr1 Knock-Out

Mouse Model of Autism. The Journal of neuroscience : the official journal of the Society for Neuroscience 37:6475-6487.

Helmchen F, Fee MS, Tank DW, Denk W (2001) A miniature head-mounted two-photon microscope. high-resolution brain imaging in freely moving animals. Neuron 31:903-912.

Hofer SB, Ko H, Pichler B, Vogelstein J, Ros H, Zeng H, Lein E, Lesica NA, Mrsic-Flogel TD (2011) Differential connectivity and response dynamics of excitatory and inhibitory neurons in visual cortex. Nature neuroscience 14:1045-1052.

Johnston DG, Denizet M, Mostany R, Portera-Cailliau C (2012) Chronic In Vivo Imaging Shows No Evidence of Dendritic Plasticity or Functional Remapping in the Contralesional Cortex after Stroke. Cerebral cortex.

Juczewski K, von Richthofen H, Bagni C, Celikel T, Fisone G, Krieger P (2016) Somatosensory map expansion and altered processing of tactile inputs in a mouse model of fragile X syndrome. Neurobiol Dis 96:201-215.

Jun JJ, Steinmetz NA, Siegle JH, Denman DJ, Bauza M, Barbarits B, Lee AK, Anastassiou CA, Andrei A, Aydin C, Barbic M, Blanche TJ, Bonin V, Couto J, Dutta B, Gratiy SL, Gutnisky DA, Hausser M, Karsh B, Ledochowitsch P, Lopez CM, Mitelut C, Musa S, Okun M, Pachitariu M, Putzeys J, Rich PD, Rossant C, Sun WL, Svoboda K, Carandini M, Harris KD, Koch C, O'Keefe J, Harris TD (2017) Fully integrated silicon probes for high-density recording of neural activity. Nature 551:232-236.

Kato HK, Asinof SK, Isaacson JS (2017) Network-Level Control of Frequency Tuning in Auditory Cortex. Neuron 95:412-423 e414.

Kleinfeld D, Ahissar E, Diamond ME (2006) Active sensation: insights from the rodent vibrissa sensorimotor system. Current opinion in neurobiology 16:435-444.

Kogan CS, Boutet I, Cornish K, Zangenehpour S, Mullen KT, Holden JJ, Der Kaloustian VM, Andermann E, Chaudhuri A (2004) Differential impact of the FMR1 gene on visual processing in fragile X syndrome. Brain 127:591-601.

La Fata G, Gartner A, Dominguez-Iturza N, Dresselaers T, Dawitz J, Poorthuis RB, Averna M, Himmelreich U, Meredith RM, Achsel T, Dotti CG, Bagni C (2014) FMRP regulates multipolar to bipolar transition affecting neuronal migration and cortical circuitry. Nature neuroscience 17:1693-1700.

Lee SH, Kwan AC, Zhang S, Phoumthipphavong V, Flannery JG, Masmanidis SC, Taniguchi H, Huang ZJ, Zhang F, Boyden ES, Deisseroth K, Dan Y (2012) Activation of specific interneurons improves V1 feature selectivity and visual perception. Nature 488:379-383.

Li N, Chen TW, Guo ZV, Gerfen CR, Svoboda K (2015) A motor cortex circuit for motor planning and movement. Nature 519:51-56.

Lissek T, Obenhaus HA, Ditzel DA, Nagai T, Miyawaki A, Sprengel R, Hasan MT (2016) General Anesthetic Conditions Induce Network Synchrony and Disrupt Sensory Processing in the Cortex. Frontiers in cellular neuroscience 10:64.

Livet J, Weissman TA, Kang H, Draft RW, Lu J, Bennis RA, Sanes JR, Lichtman JW (2007) Transgenic strategies for combinatorial expression of fluorescent proteins in the nervous system. Nature 450:56-62.

Lovelace JW, Ethell IM, Binder DK, Razak KA (2018) Translation-relevant EEG phenotypes in a mouse model of Fragile X Syndrome. Neurobiol Dis 115:39-48.

Lu H, Ash RT, He L, Kee SE, Wang W, Yu D, Hao S, Meng X, Ure K, Ito-Ishida A, Tang B, Sun Y, Ji D, Tang J, Arenkiel BR, Smirnakis SM, Zoghbi HY (2016) Loss and Gain of MeCP2 Cause Similar Hippocampal Circuit Dysfunction that Is Rescued by Deep Brain Stimulation in a Rett Syndrome Mouse Model. Neuron 91:739-747.

Marco EJ, Hinkley LB, Hill SS, Nagarajan SS (2011) Sensory processing in autism: a review of neurophysiologic findings. Pediatric research 69:48r-54r.

Maruyama R, Maeda K, Moroda H, Kato I, Inoue M, Miyakawa H, Aonishi T (2014) Detecting cells using non-negative matrix factorization on calcium imaging data. Neural networks : the official journal of the International Neural Network Society 55:11-19.

Marvin JS, Borghuis BG, Tian L, Cichon J, Harnett MT, Akerboom J, Gordus A, Renninger SL, Chen TW, Bargmann CI, Orger MB, Schreiter ER, Demb JB, Gan WB, Hires SA, Looger LL (2013) An optimized fluorescent probe for visualizing glutamate neurotransmission. Nature methods 10:162-170.

Masharina A, Reymond L, Maurel D, Umezawa K, Johnsson K (2012) A fluorescent sensor for GABA and synthetic GABA(B) receptor ligands. Journal of the American Chemical Society 134:19026-19034.

Mehta AD, Jung JC, Flusberg BA, Schnitzer MJ (2004) Fiber optic in vivo imaging in the mammalian nervous system. Current opinion in neurobiology 14:617-628.

Mineault PJ, Tring E, Trachtenberg JT, Ringach DL (2016) Enhanced Spatial Resolution During Locomotion and Heightened Attention in Mouse Primary Visual Cortex. The Journal of neuroscience : the official journal of the Society for Neuroscience 36:6382-6392.

Mostany R, Portera-Cailliau C (2008) A craniotomy surgery procedure for chronic brain imaging. J Vis Exp.

Mullard A (2015) Fragile X disappointments upset autism ambitions. Nat Rev Drug Discov 14:151-153.

Niell CM, Stryker MP (2010) Modulation of visual responses by behavioral state in mouse visual cortex. Neuron 65:472-479.

O'Donnell C, Goncalves JT, Portera-Cailliau C, Sejnowski TJ (2017) Beyond excitation/inhibition imbalance in multidimensional models of neural circuit changes in brain disorders. eLife 6.

Oberle I, Rousseau F, Heitz D, Kretz C, Devys D, Hanauer A, Boue J, Bertheas MF, Mandel JL (1991) Instability of a 550-base pair DNA segment and abnormal methylation in fragile X syndrome. Science (New York, NY) 252:1097-1102.

Okun M, Steinmetz N, Cossell L, Iacaruso MF, Ko H, Bartho P, Moore T, Hofer SB, Mrsic-Flogel TD, Carandini M, Harris KD (2015) Diverse coupling of neurons to populations in sensory cortex. Nature 521:511-515.

Ollerenshaw DR, Zheng HJV, Millard DC, Wang Q, Stanley GB (2014) The adaptive trade-off between detection and discrimination in cortical representations and behavior. Neuron 81:1152-1164.

Orefice LL, Zimmerman AL, Chirila AM, Sleboda SJ, Head JP, Ginty DD (2016) Peripheral Mechanosensory Neuron Dysfunction Underlies Tactile and Behavioral Deficits in Mouse Models of ASDs. Cell 166:299-313.

Pakan JM, Lowe SC, Dylda E, Keemink SW, Currie SP, Coutts CA, Rochefort NL (2016) Behavioral-state modulation of inhibition is context-dependent and cell type specific in mouse visual cortex. eLife 5.

Petersen CC (2007) The functional organization of the barrel cortex. Neuron 56:339-355.

Pettit DL, Wang SS, Gee KR, Augustine GJ (1997) Chemical two-photon uncaging: a novel approach to mapping glutamate receptors. Neuron 19:465-471.

Piccolino M (1997) Luigi Galvani and animal electricity: two centuries after the foundation of electrophysiology. Trends in neurosciences 20:443-448.

Pieretti M, Zhang FP, Fu YH, Warren ST, Oostra BA, Caskey CT, Nelson DL (1991) Absence of expression of the FMR-1 gene in fragile X syndrome. Cell 66:817-822.

Pnevmatikakis EA, Soudry D, Gao Y, Machado TA, Merel J, Pfau D, Reardon T, Mu Y, Lacefield C, Yang W, Ahrens M, Bruno R, Jessell TM, Peterka DS, Yuste R, Paninski L (2016) Simultaneous Denoising, Deconvolution, and Demixing of Calcium Imaging Data. Neuron 89:285-299.

Pologruto TA, Sabatini BL, Svoboda K (2003) ScanImage: flexible software for operating laser scanning microscopes. Biomed Eng Online 2:13.

Ramirez A, Pnevmatikakis EA, Merel J, Paninski L, Miller KD, Bruno RM (2014) Spatiotemporal receptive fields of barrel cortex revealed by reverse correlation of synaptic input. Nature neuroscience 17:866-875.

Reddy KS (2005) Cytogenetic abnormalities and fragile-X syndrome in Autism Spectrum Disorder. BMC medical genetics 6:3.

Ringach DL, Malone BJ (2007) The operating point of the cortex: neurons as large deviation detectors. The Journal of neuroscience : the official journal of the Society for Neuroscience 27:7673-7683.

Robertson CE, Baron-Cohen S (2017) Sensory perception in autism. Nat Rev Neurosci 18:671-684.

Rochefort NL, Garaschuk O, Milos RI, Narushima M, Marandi N, Pichler B, Kovalchuk Y, Konnerth A (2009) Sparsification of neuronal activity in the visual cortex at eye-opening. Proc Natl Acad Sci U S A 106:15049-15054.

Runyan CA, Sur M (2013) Response selectivity is correlated to dendritic structure in parvalbumin-expressing inhibitory neurons in visual cortex. The Journal of neuroscience : the official journal of the Society for Neuroscience 33:11724-11733.

Sato M, Kawano M, Ohkura M, Gengyo-Ando K, Nakai J, Hayashi Y (2015) Generation and Imaging of Transgenic Mice that Express G-CaMP7 under a Tetracycline Response Element. PloS one 10:e0125354.

Simons DJ (1985) Temporal and spatial integration in the rat SI vibrissa cortex. Journal of neurophysiology 54:615-635.

Sinclair D, Oranje B, Razak KA, Siegel SJ, Schmid S (2017) Sensory processing in autism spectrum disorders and Fragile X syndrome-From the clinic to animal models. Neurosci Biobehav Rev 76:235-253.

Sofroniew NJ, Flickinger D, King J, Svoboda K (2016) A large field of view two-photon mesoscope with subcellular resolution for in vivo imaging. eLife 5.

Tanaka M, Sun F, Li Y, Mooney R (2018) A mesocortical dopamine circuit enables the cultural transmission of vocal behaviour. Nature 563:117-120.

Telias M (2019) Molecular Mechanisms of Synaptic Dysregulation in Fragile X Syndrome and Autism Spectrum Disorders. Frontiers in molecular neuroscience 12:51.

Thompson SM, Kallarackal AJ, Kvarta MD, Van Dyke AM, LeGates TA, Cai X (2015) An excitatory synapse hypothesis of depression. Trends in neurosciences 38:279-294.

Ugolini G (1995) Specificity of rabies virus as a transneuronal tracer of motor networks: transfer from hypoglossal motoneurons to connected second-order and higher order central nervous system cell groups. The Journal of comparative neurology 356:457-480.

van der Bourg A, Yang JW, Reyes-Puerta V, Laurenczy B, Wieckhorst M, Stuttgen MC, Luhmann HJ, Helmchen F (2017) Layer-Specific Refinement of Sensory Coding in Developing Mouse Barrel Cortex. Cerebral cortex (New York, NY : 1991) 27:4835-4850.

Van der Molen MJ, Van der Molen MW, Ridderinkhof KR, Hamel BC, Curfs LM, Ramakers GJ (2012) Auditory and visual cortical activity during selective attention in fragile X syndrome: a cascade of processing deficiencies. Clin Neurophysiol 123:720-729.

van Karnebeek CD, Bowden K, Berry-Kravis E (2016) Treatment of Neurogenetic Developmental Conditions: From 2016 into the Future. Pediatric neurology 65:1-13.

Vogelstein JT, Packer AM, Machado TA, Sippy T, Babadi B, Yuste R, Paninski L (2010) Fast nonnegative deconvolution for spike train inference from population calcium imaging. Journal of neurophysiology 104:3691-3704.

Walker AS, Burrone J, Meyer MP (2013) Functional imaging in the zebrafish retinotectal system using RGECO. Frontiers in neural circuits 7:34.

Wang Y, Xu C, Xu Z, Ji C, Liang J, Wang Y, Chen B, Wu X, Gao F, Wang S, Guo Y, Li X, Luo J, Duan S, Chen Z (2017) Depolarized GABAergic Signaling in Subicular Microcircuits Mediates Generalized Seizure in Temporal Lobe Epilepsy. Neuron 95:92-105.e105.

Wassink TH, Piven J, Patil SR (2001) Chromosomal abnormalities in a clinic sample of individuals with autistic disorder. Psychiatric genetics 11:57-63.

Wei D, Yang J, Li W, Wang K, Zhang Q, Qiu J (2014) Increased resting functional connectivity of the medial prefrontal cortex in creativity by means of cognitive stimulation. Cortex; a journal devoted to the study of the nervous system and behavior 51:92-102.

Zariwala HA, Borghuis BG, Hoogland TM, Madisen L, Tian L, De Zeeuw CI, Zeng H, Looger LL, Svoboda K, Chen TW (2012) A Cre-Dependent GCaMP3 Reporter Mouse for Neuronal Imaging In Vivo. The Journal of neuroscience : the official journal of the Society for Neuroscience 32:3131-3141.

Zhang Y, Bonnan A, Bony G, Ferezou I, Pietropaolo S, Ginger M, Sans N, Rossier J, Oostra B, LeMasson G, Frick A (2014) Dendritic channelopathies contribute to neocortical and sensory hyperexcitability in Fmr1(-/y) mice. Nature neuroscience 17:1701-1709.